2018-06-04

Storing Quantum Correlations in Different Rare Earth Ion-doped Solids. A Tale of Two Memories.

Davidson, Jacob H.

UNIVERSITY OF CALGARY

Storing Quantum Correlations in Different Rare Earth Ion-doped Solids.

A Tale of Two Memories.

by

Jacob H. Davidson

A THESIS

SUBMITTED TO THE FACULTY OF GRADUATE STUDIES

IN PARTIAL FULFILLMENT OF THE REQUIREMENTS FOR THE

DEGREE OF MASTER OF SCIENCE

GRADUATE PROGRAM IN PHYSICS AND ASTRONOMY

CALGARY, ALBERTA

June, 2018

Abstract

Quantum networks of the future will be required to span the globe and interconnect many different real world systems employed by different commercial, academic, and government users. Thus, an important measure of such a network's capacity will be its ability to interact with and distribute entanglement among different mediums and devices with potentially disparate properties. Few experiments have to date shown this sort of interconnectivity between different systems with different atomic species. Here I will present our demonstration of a system in which we store two correlated photons in solid state quantum memories implemented in different rare earth ion-doped materials using the atomic frequency comb protocol. The photon pairs are generated through a spontaneous parametric down-conversion process with their wavelengths chosen to be compatible with quantum repeater implementations. One member, with a wavelength at 795 nm, is stored in an Tm:$LiNbO_3$ crystal while, simultaneously, the other member, generated at 1535 nm wavelength, is stored in an amorphous erbium doped optical fiber. The measured cross-correlation function between the recalled photons is $g^{(2)} = 16 \pm 2$, which verifies that the non-classical correlations are preserved and were present during the storage of both photons. The two storage mediums are diverse not only in terms of their different photon acceptance wavelengths, but also with regards to the material properties as hosts for the dopant rare-earth ions. Our results show that quantum nodes and networks based on fundamentally different systems can be interfaced to distribute entanglement.

Acknowledgments

I would like to thank, first and foremost, my group here in Calgary. For the past few years you have been my friends and family; the people that I start and end every day with. Everyone in the QC2 Lab has made a huge difference to my work, and my life here in Calgary. Specifically, I would like to thank Marcel.li, Neil, and Daniel for being the ones to train me in almost all of my hard skills in lab. You three have made me the (semi) qualified experimentalist that I am today. Wolfgang you were instrumental in guiding me upon the correct path for where to place my goals and expend my efforts. I will always remember your processes on how to approach a problem. Mohsen and Gustavo, you were there with me everyday during a few months of data collection, and you made sitting in a dark lab much, much more fun. Raju and Thomas, you are some of the best lab and office mates I could hope to have. If we got out skiing, or climbing as much as we had discussed, I would never have finished this degree on time. We seem to have mostly gone separate ways for now, but I hope to work with all of you again going forwards.

While my lab group was hugely helpful, I also could not have completed this degree without close friends and family. Alex Cates, Andrew Szakowski, and David DeLeon you are the ones who were told more about my research than you would ever have wanted to know. Alex Ciolko, through easy days, tough days, and everything in between, you have with your tongue sticking out and a smile on your face encouraged me, my work, and what I tried to put into this degree. Steven and Mimi, I couldn't have hoped to find a better local family contingent in Calgary. You were a surprise, and you have been amazing. Finally, Karen and Marc, thank you for the years of education that you provided for me. I am going to keep going, but I could never have reached this point, or beyond, without your love and support.

Thank you all.

Table of Contents

List of Figures and Illustrations

List of Symbols, Abbreviations and Nomenclature

Symbol	Definition
U of C	University of Calgary
REI	Rare Earth Ion
RWA	Rotating Wave Approximation
EIT	Electromagnetically Induced Transparency
CRIB	Controlled Reversible Inhomogeneous Broadening
GEM	Gradient Echo Memory
AFC	Atomic Frequency Comb
SHG	Second Harmonic Generation
SPDC	Spontaneous Parametric Down Conversion
SNSPD	Superconducting Nano-wire Single Photon Detector
TDC	Time to Digital Converter
CW	Continuous wave
AOM	Acousto-Optic Modulator
PM	Phase Modulator
AWG	Arbitrary Waveform Generator
MEMS	Micro Electro-Mechanical Switch
PC	Polarization Controller
SNR	Signal to Noise Ratio
CAR	Coincidence to Accidental Ratio

Chapter 1

Introduction

1.1 Quantum Mechanics

As technological advances over the years have made control of macroscopic objects easier we have also begun to harness microscopic objects found in nature. As we innovate in our control of objects as small as a single atom, we must turn to quantum mechanics as a way to explain and predict the world we seek to command. Since its inception, quantum mechanics has struck some of the greatest minds as odd or incomplete [1], but it is exactly those oddities of the theory that we now look to exploit and control. Quantum mechanics' fundamental differences from classical mechanics can be summarized with a few key principles, the very same that lead to the newfound power in quantum technology[2].

In the most complete manner, quantum systems are described by wave functions that characterize their behavior. The wave function of a quantum system may represent the system as a "blend" of many different states which we then define using the most convenient basis. This is called the principle of superposition as many basis states can interfere with one another as waves do causing macroscopic consequences for measurements of the system. Additionally a wave function may define a quantum system that encompasses the shared state of multiple sub-systems. In some cases these states can only be characterized as a whole instead of as a product of their individual sub-systems. Known as an entangled states, this is a purely quantum feature as there is no classical analog for systems that act in this manner. Many improvements to modern technology rely on these unique properties of quantum mechanics and the effects they cause to the macroscopic world[2].

1.2 Quantum Information

The benefits to be derived from quantum technologies are untold, just as it was impossible to predict how dominant the computer would become in today's society. Some quantum technologies are already in use today and show great potential to improve many of the aspects of our classical electronics technology. There exist schemes for quantum computation such as Shor's algorithm that will enable us to solve problems that classically could take a lifetime to compute [3]. In terms of communication, quantum devices show benefits when it comes to security of information being transmitted using various QKD protocols[4]. These advances and more will be implemented using quantum processors and quantum networks.

In the same way that classical computers operate on the basis of the logical bit, the basic building block of quantum information is the quantum bit(qubit). Analogous to a classical bit, which can be either 0 or 1, the qubit is the state of a wave function defined by $|\psi\rangle = \alpha|0\rangle + \beta|1\rangle$ where the complex probability amplitudes α and β obey $|\alpha|^2 + |\beta|^2 = 1$ and the two kets ,$|0\rangle$ and $|1\rangle$, represent two states that form a basis for the system. Hence, a qubit can represent infinitely many more states than a single classical bit as there are infinite combinations, superpositions, of the basis states available instead of a fixed two. Adding more qubit terminology, an entangled state is one that cannot be described as a product state. For example, given states

$$|\psi\rangle = |10\rangle + |11\rangle = |1\rangle \otimes \Big(|0\rangle + |1\rangle\Big) \tag{1.1}$$

$$|\varphi\rangle = |00\rangle + |11\rangle, \tag{1.2}$$

we can see that $|\psi\rangle$ is a product state because it is a tensor product of different states, while $|\varphi\rangle$ is an entangled state because it is not a product state yet it still describes multiple sub-systems.

Using qubits as elementary units of information we can take advantage of their quantum nature by using superposition and entanglement in the operations that we perform on the

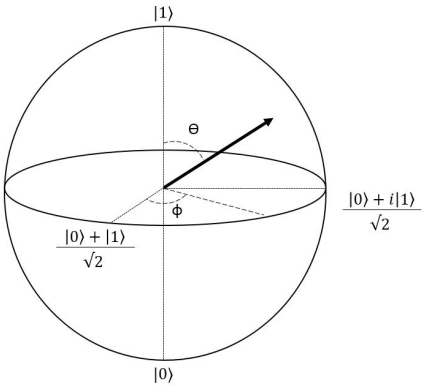

Figure 1.1: The Bloch Sphere allows for a good visual representation of a qubit. The state of the qubit can be defined by the angles that create a unit vector that points from the origin to the surface of the sphere $|\psi\rangle = \alpha|0\rangle + \beta|1\rangle = \cos(\theta/2)|0\rangle + e^{i\phi}\sin(\theta/2)|1\rangle$. Theta determines the relative amplitudes of the two basis states while Phi defines the phase between the two components of the vector.

systems in question. Similarly since the interaction between different qubits is the interaction between two different quantum mechanical wave functions they can also interfere. This turns out to be a key factor for the improvement of computing speeds in quantum computing. In fact, the quantum nature of the qubit can be seen by its broader mathematical definition compared to a classical bit. This allows for a broader set of problems to be solved efficiently and effectively[5].

Much of what we understand about quantum information processing and quantum communication has been determined using theoretically ideal qubit systems. The logical bits of a classical computer are carried out using transistors, but physicists are still perfecting many different quantum systems that are promising candidates for establishing qubits. Real qubits face a number of different experimental challenges before the benefits of quantum information science can be fully exploited. An ideal qubit should have limited interaction with its environment which tends to destroy the fragile quantum state (decoherence), yet it should be easy to prepare and read out when necessary. Other requirements are detailed in the DiVincenzo Criteria, [6], that help to define what is required from a physical implemen-

tation of a qubit. There are few physical systems that satisfy all of these requirements at once so it becomes more effective to select which requirements are needed to perform a given task. Certain implementations of qubits have already become clear leaders in their ability to perform certain computational or networking tasks; for example the superconducting qubit for quantum information processing [7], and photons for quantum communication. The crucial experimental tasks at hand are to both improve the benefits of each of these separate systems, but also to perfect the ability to connect them with one another.

As we develop devices for communication and computation based on different types of qubits, it will become useful to link these together, as we have done with our classical telecommunications networks, to form the quantum Internet[8]. The classical Internet functions by connecting many different classical devices at a distance. Thus, quantum communication and the ability to move qubits over large distances becomes essential for a quantum internet. This task requires some variations from its classical counterpart to support the quantum nature of the information being transmitted. There are a number of different schemes proposed for long distance quantum communication, transmission of entanglement, and transmission of qubits over distances larger than 100-200 km that rely on single photons as information carrying qubits[9, 10].

Photons are the fundamental particle of light, and they can be turned into qubits using any of their many different degrees of freedom [11]. They travel at $c = 3 \times 10^8 m/s$ (in free space) leading to large communication rates, and they are robust against decoherence and environmental influences. Entanglement is an innately quantum way of describing the connection between objects, as it defines them as smaller parts of a larger interconnected quantum system. By showing that our various systems are parts of an entangled state, or that they share distinct quantum correlations, we can show that we have successfully connected the different quantum devices.

1.3 Interfacing Quantum Technology

With photons chosen as a mediator for connecting different devices there are still differences between systems that need to be bridged. One way in which many systems differ is simply the operating wavelength of the photons that they can interact with. For example three leading systems, microwave photons for control of superconducting circuits[7], light at ≈ 600 nm for working with NV centers[12], or light at at ≈ 800 nm for Thulium based quantum memories,[13], are all driven by very different frequencies of electromagnetic radiation. All these wavelengths are again different from the optimal transmission wavelength, 1.5 μm, used in low-loss optical telecommunications infrastructure. Any interfacing of different quantum systems is useful in that it paves the way for multifaceted quantum systems to become a reality. Thus far there have been a few experiments that sought to connect disparate quantum systems [14, 15, 16]. These works have shown conversions in wavelength for single photons, and thus potential for connecting two very different qubit implementations.

We carry out a proof of principle experiment to show quantum correlations between two different rare earth crystals mediated by a pair of correlated single photons. Using two temporally correlated photons from a photon pair source, we send one to a thulium based quantum memory and one to an erbium based quantum memory. Thulium based quantum memories have been shown to be promising candidates for storage of quantum information. Erbium materials have merit both as quantum memories, and as possible transducers for quantum connection to superconducting qubits and the microwave regime. We store both photons of the pair simultaneously in the two different materials until they are re-emitted after a given storage time and sent to single photon detectors. We show that the non-classical correlations between the photon pairs are intact following the storage and indicate successful linkage of two unique quantum memories.

The correlation statistics are gaged by the cross-correlation function $g^{(2)}$, and its measurement is the key result discussed in this thesis. The measurement requires precise synchro-

nization between the different parts of the setup and for all components to work optimally. This experiment involves a photon pair source to generate correlated single photons. To store those photons we use rare earth crystals and fibers that operate efficiently in a cryostat at a few hundred milli Kelvin temperatures. Finally we use highly efficient single photon detectors and a large array of electronics to manage all the signals and synchronize the timing for the entire setup. The final goal is to show entanglement between these different quantum systems, and an important step on the way is to measure non-classical photon-number correlations between the systems.

This manuscript is organized in the following manner. In Chapter 2, I will describe some basics of light matter interaction processes that we use to make quantum memories. Chapter 3 will be a brief review of quantum memories, and the scheme that we use for storing single photons in this experiment. In Chapter 4, I will give an in depth summary of our experimental setup and our optimization procedures for this experiment. Chapter 5 details some preliminary results, and the final result of the $g^{(2)}$ measurement that we have produced. Finally in chapter 6, I will discuss experimental improvements, subsequent demonstrations of entanglement between the two systems, and their importance in the context of quantum information and quantum networking.

1.4 Author Contributions

The experiment detailed in this thesis was carried out by a number of different lab members. Marcel.li Grimau Puigibert developed and characterized the entangled photon pair source, managed the analysis electronics for detection of the single photons, and taught me much of what I learned to work with for this experiment. Gustavo C. Amaral maintained the entangled photon pair source and worked on parts of the data collection electronics and analysis after Marcel.li's departure. Mohsen Falamarzi Askarani, with help from Thomas Lutz, operated the erbium memory setup. Daniel Oblak was instrumental with hands on

work throughout different areas of the setup, and valuable discussion for all of the different components. Neil Sinclair was part of many discussions and gave crucial input for many parts of the experiment. They each taught me much about operating my portions of the setup, which I will summarize next. Wolfgang Tittel supervised the work and directed us towards the best possible measurements and improvements to make.

My portion of work for the experiment was to run the thulium memory. This involved optical alignment of the different components and our 795 nm laser diode to generate the quantum memory. I partially assembled and maintained the electronics to run different optical pulse sequences and link to the rest of the setup. Though we run the thulium memory in a specific configuration I also performed a number of initial experimental investigations to find these optimal conditions with which we have collected all of our data. I took a large part in getting the cryostat and single photon detector components functioning correctly for our measurements. Finally, I re-wrote portions of the data collection and analysis software that we used for initial runs of the experiment and many of our preliminary results.

Chapter 2

Light-matter Interaction

2.1 Mathematical Description of Light

To begin a description of light we must start with the very basics of the electromagnetic field. Everything understood about classical electromagnetism can be seen through careful inspection and manipulation of Maxwell's Equations.

$$\nabla \cdot \mathbf{E} = \frac{1}{\epsilon_0}\rho \tag{2.1}$$

$$\nabla \times \mathbf{E} = -\frac{\partial \mathbf{B}}{\partial t} \tag{2.2}$$

$$\nabla \cdot \mathbf{B} = 0 \tag{2.3}$$

$$\nabla \times \mathbf{B} = \mu_0 \mathbf{J} + \mu_0 \epsilon_0 \frac{\partial \mathbf{E}}{\partial t} \tag{2.4}$$

Denoted here is a complete free-space classical description of the electric field $\mathbf{E}$, and magnetic field $\mathbf{B}$ in terms of charge density ρ, current density $\mathbf{J}$, and the permittivity and permeability of free space ϵ_0 and μ_0 respectively. With no current or charge density ($\mathbf{J} = 0,\ \rho = 0$) we can take the curl of 2.2 and 2.4 above, and through the vector identitiy $\nabla \times (\nabla \times \mathbf{A}) = \nabla(\nabla \cdot \mathbf{A}) - \nabla^2 \mathbf{A}$ we can see that wave equations for the fields appear.

$$\nabla^2 \mathbf{E} = \mu_0 \epsilon_0 \frac{\partial^2 \mathbf{E}}{\partial t^2} \tag{2.5}$$

$$\nabla^2 \mathbf{B} = \mu_0 \epsilon_0 \frac{\partial^2 \mathbf{B}}{\partial t^2}. \tag{2.6}$$

Mathematically, electromagnetic waves are the solutions to these wave equations. In a physical sense, light can be seen as waves of electromagnetic fields propagating through space at the speed $c = 1/\sqrt{\mu_0 \epsilon_0}$.

We can define the wavenumber k, from the wavelength λ, as $k = 2\pi/\lambda$, and $\mathbf{k}$ as the wavevector with magnitude k and pointing in the direction of the light waves propagation.

This leads to common solutions to the wave equations in free space and in materials called the plane waves, which are given by,

$$\mathbf{E}(z,t) = \mathbf{E_0}(z,t)e^{i(kz-\omega t)}\mathbf{e} \tag{2.7}$$

$$\mathbf{B}(z,t) = \frac{1}{c}\mathbf{k}\times\mathbf{E}. \tag{2.8}$$

We have folded the vector components of the field into the complex field vector $\mathbf{E}_0(z,t)$ denoting a slowly varying envelope for the wave. The frequency is $\omega = ck$, the electric field amplitude points in the $\mathbf{e}$ direction denoting the polarization, and the wave is propagating in the z direction. Using this description, we can understand how classical light is employed to change the states of isolated atoms or ions free space.

There have also been numerous experiments that have proven, and gone on to utilize, the quantum nature of light [17]. As single photons are a valuable resource for quantum information transmission and processing, we focus on the storage of single photons in our quantum memories. To understand these experiments we need to expand the equations above through quantum states and canonical quantization. The single photon nature of our stored light can be established quantitatively by the normalized cross-correlation $g^{(2)}$ function which sets an upper bound for fields compared to light particles [18].

2.2 The Atoms of Choice

Thulium and erbium are known as rare earth (RE) elements and although not as rare as once thought, they belong to a group of 15 elements that have become essential in technological applications and modern electronics. For quantum information applications specifically, the selection rules for the $4f$ orbital electrons in these REI give them good properties when they are bound in solid state crystals. More precisely, erbium and thulium have 68 and 69 electrons, respectively, which fill orbitals that extend far from the nucleus. When placed in a crystal, these trivalent ions are generally held in place by bonds that empty out electrons from

their outermost $6s$ orbital. This leaves a core of other electronic transitions that are shielded from the greater environment of the crystal structure and chemical bonding interactions. Though selection rules prevent the $4f \rightarrow 4f$ electronic transitions, they are addressable and show good properties in terms of line-width and coherence when the ions are dopants in solid state crystals. This makes them good approximations of single ions even with the crystal environment around them [19].

The energy level structure of our choice REIs can then be described including these shifts with their quantum numbers by the convention $^{2S+1}L_J$, where S is the spin quantum number for the multi-electron system assuming LS coupling, L is the total angular momentum quantum number (e.g. $L = 0$ is an S orbital), and J is the orbital angular momentum quantum number. Different hyperfine levels have different spin quantum numbers, while different stark levels correspond to different orbital quantum numbers. For the erbium atoms that we address, we use a pair of hyperfine levels the $^4I_{15/2} \leftrightarrow ^4 I_{13/2}$ transition as seen in Fig. 2.1 [20]. In the thulium case we use the $^3H_6 \leftrightarrow ^3 H_4$ transition between hyperfine levels that are split from the lowest possible Stark level [13]. However, we still need to account for certain environmental effects that split and shift the energy levels compared to what they would be in a single isolated ion.

The first of these effects is the Stark shift, caused by a static electric field from the environment of the crystal. These Stark shifts depend heavily on the symmetries in the crystal and there exist many models outside of the scope of this thesis for determining the exact spectra of these shifts. If the ions have a permanent dipole moment, we can also control the Stark shifts present in the material with the addition of external electric fields. Another phenomenon to alter the level structure of our ions is the Zeeman splitting caused by an applied magnetic field which creates hyperfine levels in the energy level structure. It has been shown that our thulium crystal exhibits ground state level splitting of 1.3 GHz/T when an external magnetic field is applied [22]. The erbium doped fiber we use has splitting

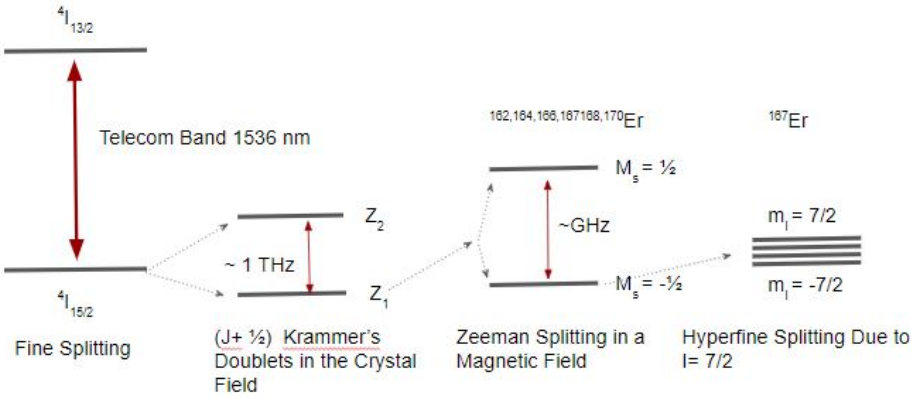

Figure 2.1: Erbium^{3+} ion level diagram including different splittings. Electronic levels, given by the term symbol $^{2S+1}L_J$ (where S, L and J denote, respectively, the spin, angular momentum and total angular momentum of the trivalent ion) are split into J+1/2 Stark levels. These doublets are further split into Zeeman levels, and, for the ^{167}Er isotope, into 2I+1 hyperfine levels (where I=7/2 is the isotope's nuclear spin). Figure adapted from [21]

of 150 GHz/T between the hyperfine levels [20]. With these shifts taken into account, we have a good understanding of the energy level spectrum for the erbium and thulium atoms that we are interested in utilizing for quantum memory.

2.3 Light-matter Interaction

This thesis is focused on manipulation and storage of light in a solid state atomic quantum memory. With the above definitions, we can embark on a deeper theoretical description of how the individual atoms in our Erbium and Thulium ensembles interact with an incident light field. We will focus in this section on the ability of an external light field to change the state of the atomic system. Following some of the derivations in [23] and [24], we will highlight their connections to the optical pumping process we use for preparing our quantum memory.

First we restrict the theory to that of a two level atom with a ground state $|g\rangle$ and an excited state $|e\rangle$, separated by a energy difference $\hbar\omega_{eg}$. This is of course not a complete

picture, but when the incident electric field is tuned to be close to the resonance frequency, ω_{eg}, it is valid to ignore other transitions. The atomic state can then be described by

$$|\psi\rangle = c_e|e\rangle + c_g|g\rangle \tag{2.9}$$

where c_g and c_g are the complex probability amplitudes for the ground and excited levels, respectively. The isolated two-level system can be treated with the same quantum mechanical framework that allows treating spin 1/2 particles, the polarization states of light, and more.

In the absence of interactions, the state of this isolated two dimensional atomic system in time can be described by the Hamiltonian

$$H_A = E_e|e\rangle\langle e| + E_g|g\rangle\langle g| = \begin{pmatrix} E_g & 0 \\ 0 & E_e \end{pmatrix} \tag{2.10}$$

where energies E_e and E_g are the energies of the ground and excited states and $\hbar$ is Planck's constant such that $E_e - E_g = \hbar\omega_{eg}$. We are interested in how the electric fields described earlier will change the atomic state, so a Hamiltonian with only the terms defining the atomic energy levels will not suffice. To do this we must add other terms to the Hamiltonian to account for the newly introduced electric field interacting with the energy levels of the atom. The interaction term is given by the expression for the energy of an electronic dipole in an electromagnetic field,

$$H_I = -\mathbf{d}\cdot\mathbf{E} \tag{2.11}$$

$$\mathbf{d} = \begin{pmatrix} 0 & d_{eg} \\ d_{eg}^* & 0 \end{pmatrix} \tag{2.12}$$

where $\mathbf{d}$ is the dipole moment operator of the atom (with elements d_{eg}, d_{eg}^*) and $\mathbf{E}$ is the electromagnetic field evaluated at the location of the atomic dipole. Note that the zero components of this dipole operator are due to symmetry assumptions that may not apply in a solid state medium. This can be accounted for by including the Stark shifts, discussed above, in the model. I will not follow this approach going forwards for simplicity sake. The

electric field for the interaction in the medium is given by the plane wave solutions from 2.7 with real and complex components.

$$\mathbf{E}(z,t) = \frac{1}{2}\left(\mathbf{E_0}^*(z,t)e^{i\omega t} + \mathbf{E_0}(z,t)e^{-i\omega t}\right). \tag{2.13}$$

Then the total Hamiltonian becomes

$$H = H_A + H_I \tag{2.14}$$

Using the rotating wave approximation (RWA) to neglect components that oscillate too quickly we can then apply the Schroedinger or Heisenberg equation to determine the time evolution of our atomic state based on this new Hamiltonian.

This approach leads to equations of motion for the probability amplitudes of the ground state c_g and of the excited state c_e,

$$\frac{\partial}{\partial t}c_e = \frac{-i\omega_{eg}c_e}{2} - \frac{id_{eg}\mathbf{E}e^{-i\omega t}c_g}{2\hbar} \tag{2.15}$$

$$\frac{\partial}{\partial t}c_g = \frac{i\omega_{eg}c_g}{2} - \frac{id_{eg}^*\mathbf{E}e^{i\omega t}c_e}{2\hbar}. \tag{2.16}$$

It is clear from these equations that the time evolution of the atomic states are now coupled to one another via the electric field, which drives changes in the probability amplitude of the ground and excited states. We can simplify these equations of motion by assuming the incident field is exactly on resonance with the transition in question, and performing a change of variables defining $C_{e,g} = c_{e,g}e^{\pm i\omega t/2}$. When we begin with the atom in the ground state, this leads us to simpler equations of motion,

$$\frac{\partial^2}{\partial t^2}C_e = -(\frac{\Omega_r}{2})^2 C_e \tag{2.17}$$

$$\frac{\partial^2}{\partial t^2}C_g = -(\frac{\Omega_r}{2})^2 C_g \tag{2.18}$$

with probabilities

$$|C_g(t)|^2 = \cos^2(\frac{\Omega_r}{2}t) \tag{2.19}$$

$$|C_e(t)|^2 = \sin^2(\frac{\Omega_r}{2}t) \tag{2.20}$$

and $\Omega_r = d_{eg}^* \hat{\mathbf{E}}/\hbar$ the Rabi frequency. Thus, the probability of an atom being in the excited or ground state varies sinusoidally with the length of time for which the electric field is applied. After applying a field for a duration of time such that $\Omega_r t = \pi$, the level population has gone through a half cycle from ground to excited state, a so called π-pulse. In this way we can control the population difference of the energy levels that are on resonance with the laser frequency that we apply by applying laser pulses of different durations.

This same process detailed above can be repeated when adding other terms to the Hamiltonian. One such complication better describes the reaction of an atom that is not entirely isolated from a bath of thermal field modes. This involves a statistical treatment of the system starting with the density matrix for the two level atomic system.

$$\rho = |\psi\rangle\langle\psi| = \begin{pmatrix} \rho_{ee} & \rho_{eg} \\ \rho_{eg}^* & \rho_{gg} \end{pmatrix} \tag{2.21}$$

Repeating the RWA with the slightly modified Hamiltonian results in the optical Bloch equations [25].

$$\dot{\rho_{eg}} = -\Big(\frac{1}{2T_2} - i\omega_{eg}\Big)\rho_{eg} + \frac{1}{2i\hbar} d_{eg} \mathbf{E_0}^* I \tag{2.22}$$

$$\dot{I} = -\frac{I - I_0}{T_1} + \frac{1}{i\hbar}\Big(d_{eg}^* \mathbf{E_0} \rho_{eg} - d_{eg} \mathbf{E_0}^* \rho_{eg}^*\Big). \tag{2.23}$$

Here I_0 is the equilibrium inversion due to the the thermal bath of field modes. Here ρ_{eg} is the expectation value for the atomic dipole, and $I = \rho_{ee} - \rho_{gg}$ the inversion, is the population difference between the excited and ground levels. These two quantities show the same coupling between atomic states and the driving electric field as seen in the equations of motion above for the state probability amplitudes.

The difference to be noted here is the appearance of time constants T_1 & T_2, which arise from the atom coupling to the vacuum modes available. The T_1 time constant is the energy relaxation time for the system to return to its equilibrium state for a given temperature of the environment. With more thermal energy in the system, the time to reach equilibrium is

shortened. The time constant T_2 is the coherence time for the electric dipole, and is limited by effects that disturb the phase of the two state system, and ultimately by the population decay time such that $T_2 \leq 2T_1$. These relaxation effects determine the time scales on which we can control the population of a given atom or ensemble, and they set the fundamental limits on some of the storage abilities in atomic media.

2.4 Optical Pumping

The previous sections have served to show how the state of an atom changes when exposed to light on resonance with one of the atomic transitions. By adding more atomic levels we can change how the system evolves. Using the Zeeman level splitting mentioned in section 2.2, we can split the ground and excited levels of our atomic system into multiple levels with different energies. In this multi-level system, the atom will decay from the excited states into the same or a different Zeeman level with different probabilities. Using an electromagnetic field on resonance with one ground-to-excited-state transition we use the population control seen from equations (2.17) and (2.18) to move the atom into the excited state . If the atom decays into the original ground state then it will be transferred back to the excited state. Repetition will eventually result in the atom decaying into another ground state created by the Zeeman splitting. The pumping light is now off resonant with the transition back to the excited state, hence the atom remains in this auxiliary ground state until population relaxation occurs. This optical pumping technique will become useful in creating our quantum memories. Section 3.2.4 will discuss how it translates from a single atom to the ensemble of atoms seen in a REI crystal.

Chapter 3

Quantum Memories

3.1 Figures of Merit

It is useful to understand the systems used in this experiment in the context of the broader field of reversible optical quantum memories. Such memories operate by storing either single photons or coherent light pulses that are provided from a separate source. By reversible storage we mean the transfer of the quantum state of the light to an atomic quantum variable and back to the light. There are a number of different schemes for creating reversible quantum memories, each of which have advantages and drawbacks depending on the application. Described below are figures of merit, that are useful in determining the effectiveness and future promise of a given reversible optical quantum memory protocol.

3.1.1 Fidelity

The fidelity of a memory is a measurement of how close the output quantum state is to the input state. Essentially, do we get out what we put in? This question is more complex when describing quantum information instead of classical bits. It requires the density matrices ρ and ρ' of the input and output states, respectively. Using both, we determine the fidelity $F(\rho)$ by

$$F(\rho) = Tr\Big(\sqrt{\sqrt{\rho'}\rho\sqrt{\rho'}}\Big). \tag{3.1}$$

Using a classical memory, is it possible to store quantum information and reproduce a qubit state with a fidelity of 2/3. Thus it is important that a true quantum memory has a fidelity well above this.

3.1.2 Efficiency

Quantum memory efficiency is a measure of energy stored versus energy re-emitted. It can also be seen as the probability of storing and retrieving an incident photon. As in the classical memory case, unit efficiency is desired for most applications, though the highest shown to date has been 87% [26]. Quantum memory schemes with an efficiency limited by fundamental or material properties to below one are unattractive for future widespread use. Note that the loss in efficiency is due to energy that is absorbed but not re-emitted, or due to energy that is transmitted through the memory without interaction.

3.1.3 Storage Time

The merit of a given storage time for a memory is largely based on application. There exist uses for quantum memories where storage times on the order of *ps* are acceptable, but in general longer storage times make for better memories. Storage time can also fall into two different categories, on demand storage, and preset storage time. Electronic computer memories create on demand storage, but this is not required for all quantum applications. Often, longer storage time results in lower fidelity and efficiency of the memory as de-phasing processes and decoherence take their toll on the stored state.

3.1.4 Bandwidth

The bandwidth of an optical pulse is related to the pulse-duration via the Fourier transform limit. For single photons have this can be seen as a result of the Heisenberg uncertainty relation. Thus a given frequency bandwidth of photon corresponds to a certain temporal duration of the photon. The transmission rates for information require single photons to be short in time, which entails a large frequency bandwidth. A quantum memory for these single photons must then be able to absorb photons at various a preferably large bandwidths. Memory bandwidths of a few GHz is desirable to achieve communication rates comparable with classical signals. In general a memory with a wider bandwidth is a better memory,

although some applications call for small bandwidth quantum memories.

3.1.5 Multi-modal Capacity

One extremely important aspect of increasing a quantum memory storage capacity is its ability to store single photons in several modes simultaneously. These modes can be separated spatially, temporally or spectrally creating different channels in space, time and frequency to transmit the information. Many applications require memories that have a high multi-mode capacity. Note that a large memory bandwidth can also be split into many spectral channels. The best memories will have a multi-modal capacity that scales independently of physically limited parameters, such as optical depth or the memory's spatial size.

3.1.6 Functional Wavelength and Implementation Complexity

As with many of the criteria above, the application of a quantum memory determines how applicable each figure of merit may be. For the case of quantum communication and the interconnection of various quantum devices, it is optimal if the quantum memory can function in the wavelength range for low loss optical fiber, i.e. 1520-1600 nm. This is not a requirement in all cases, as wavelength can be converted via nonlinear optical processes, but it increases the efficiency of a system as a whole many fold when transmission over a long distance is desired. Similarly, if the quantum memory requires a huge operational overhead, such as a cryostat, superconducting materials, or many frequency stabilized lasers to function well, it may be less desirable simply because of its difficulty.

3.2 Reversible Quantum Memory Schemes

With many different applications and a strong connection to past quantum optics research the subject of quantum memories has been well reviewed over the past few years [27, 28, 29]. Here, I will give a quick overview of the different types of reversible quantum memories

that are prevalent today. Secondly, I will describe in detail the AFC scheme for quantum memory that was used for both quantum memories in the experiment detailed in this thesis. For a very basic comparison of many different published quantum memory results, turn to Appendix A.

3.2.1 Electromagnetically Induced Transparency

Electromagnetically Induced Transparency (EIT) is a good introductory quantum memory as it was one of the first ever implemented. The principle behind EIT relies on altering the group velocity of light while it is traveling through an atomic medium. The speed of light in free space is c, but when light is passing though a material the speed of light becomes dependent on that materials index of refraction n. The group velocity of light is defined as $v_g = \frac{\partial \omega}{\partial k}$ and refers to the speed at which light can actually transmit information. Following with the definition of wave number we see that,

$$\frac{1}{v_g} = \frac{\partial k}{\partial \omega} \tag{3.2}$$

$$= \frac{\partial (n\omega/c)}{\partial \omega} \tag{3.3}$$

$$= \frac{1}{c}\left(n + \omega \frac{\partial n}{\partial \omega}\right). \tag{3.4}$$

$$\text{Thus} \quad v_g = \frac{c}{n + \omega \frac{\partial n}{\partial \omega}}. \tag{3.5}$$

Thus the group velocity depends on the index of refraction but also the dispersion of the material. The EIT memory protocol functions by creating large changes in the index of refraction over short frequency spans which then lowers the group velocity of light by many orders of magnitude.

Shown in Fig. 3.1a is the level structure for an atomic medium used for EIT. The absorption spectrum of these levels is altered with a strong coherent light beam that is on resonance with a two-level atomic transition $|aux\rangle \Leftrightarrow |e\rangle$ in the material used for storage. The control field creates a narrow transparency in the absorption line where the atoms present

cannot absorb light. From the Kramers-Kronig relations,[30], this sharp absorption feature translates into a large change in the index of refraction over a narrow frequency window. This steep slope in the index of refraction slows the group velocity of the light to be stored. As the control beam creating the transparency is then turned off adiabatically, the light gets stored as a coherence between the two grounds states present in the material [31]. By adiabatically restoring the control beam this coherence is converted back to a photon which then exits the memory.

EIT has been implemented in many different materials, making it diverse in terms of potential operating wavelengths. EIT has been used to produce some of the longest storage times, on the order of a second, of classical light and single photons [32], but there are limitations to this protocol. Since the transmission window in the absorption profile must be narrow to get large changes in group velocity, the bandwidths of the created memories are often narrow. It has also been shown that the multi-mode storage capacity of EIT scales with the square root of the optical depth $\sqrt{d}$, which is quite limiting with regards to available materials [33]. Additionally, since both the stored single photons, and the control pulse must be of similar frequency, and since they are present at the same time, it is challenging to separate the two[32]. This resultant noise on the retrieved single photon state must be filtered somehow, which increases the complexity and decreases the efficiency of most EIT quantum memory setups.

3.2.2 Off-Resonant Raman Memories

A protocol similar, but slightly different from EIT, is called a Raman memory. As seen in Figure 3.1b it utilizes a very similar level structure and the main difference is that for Raman memory, the control and input fields are off resonant from the atomic transitions. In this way, the fields create a virtual level that mediates the interaction between the atomic states and control and input fields. This technique results in higher memory bandwidth and reduced fluorescence from the excited level population, which leads to lessened noise.

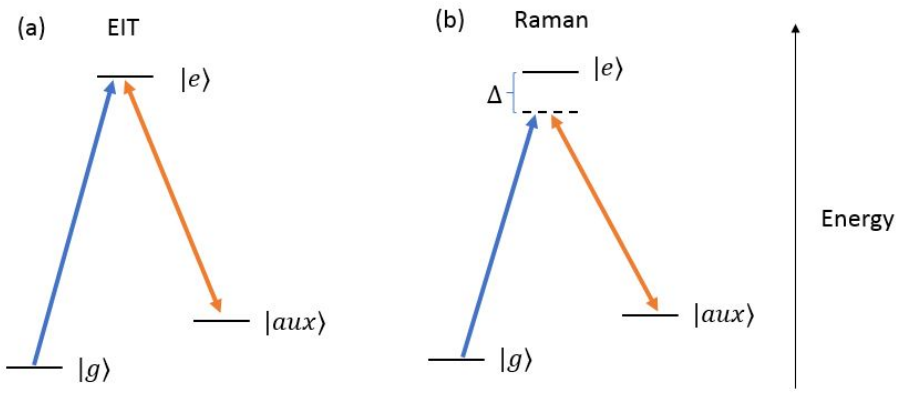

Figure 3.1: Level structures for the EIT (a) and off resonant Raman memory (b) schemes. These 3-level atomic structures are made up of the excited state $|e\rangle$, the ground state $|g\rangle$ and a secondary ground or auxiliary level $|aux\rangle$. The arrows in blue denote the input photon field, while the arrows in orange are the control fields for each process. Note that in (b) both optical fields are detuned by Δ from resonance with $|e\rangle$.

However, since the storage process is off resonance, one of the disadvantages of this scheme is the high optical control field power required for efficient reading to and writing from the memory. This excess power can lead to other nonlinear optical effects which produce noise that limits the memory fidelity[32]. Raman memories have shown promise in their ability to store single photons with large bandwidth, but they still suffer the $\sqrt{d}$ dependence in optical depth for their multi mode scalability [33].

3.2.3 Controlled Reversible Inhomogeneous Broadening

Controlled reversible inhomogeneous broadening(CRIB) or Gradient Echo Memories(GEM) both rely on similar principles of their host materials [34], namely the ability to broaden a transition line by imparting a spatially dependent shift by means of a controllable external field. This scheme relies on a sharp absorption line, which may be tailored out of an inhomogeneously broad spectrum using optical pumping. As seen in Fig. 3.2 this absorption line is modified using external electric or magnetic fields to create an artificial inhomogeneous broadening. This new controllable absorption feature is then in place as photons are sent

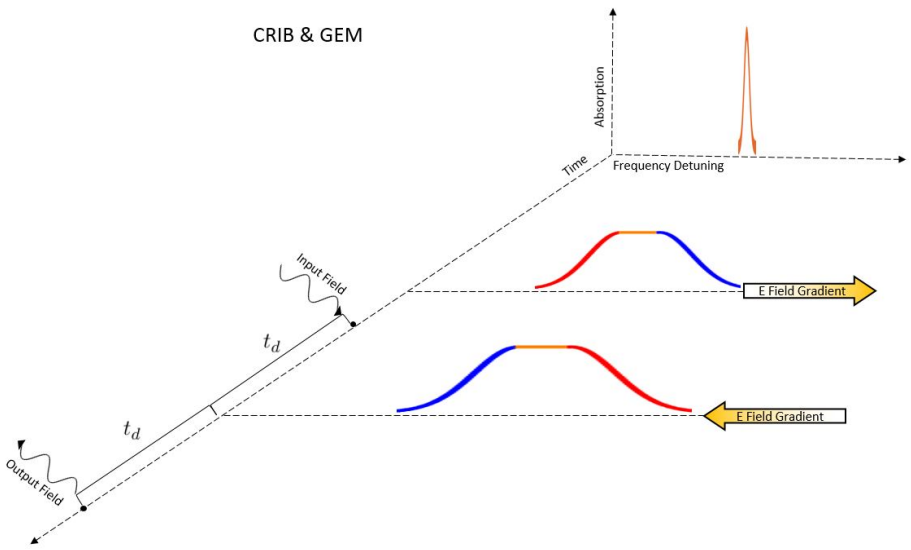

Figure 3.2: The storage scheme for CRIB and GEM are shown here. An initial narrow absorption line, either natural or created by optical pumping, has a gradient field applied to it, broadening the absorption feature over a larger range. The light to be stored in the memory is absorbed, and then, after some delay, the field gradient that creates the artificial broadening is reversed. Again after that delay time, the ensemble re-emits the stored light.

into the medium and absorbed creating a de-localized excitation in the form of a Dicke state

$$|\psi\rangle = \sum_{j=1}^{N} c_j e^{i2\pi\delta_j t} e^{-ikz_j} |g_1 ... e_j ... g_N\rangle. \tag{3.6}$$

Here the combined state of the atomic medium is given by a sum over terms which correspond to a particular atom being excited. In other words, the state is given by a superposition of all atoms in the ground state with a single excitation shared amongst them. Each term has a probability amplitude c_j and will de-phase at a rate proportional to its frequency detuning δ_j. The exponential term $e^{i2\pi\delta_j t}$ is the phase factor that each term picks up from the environmental factors including the artificial detuning due to the electric field. To trigger reemission after the atoms have been allowed to de-phase for a certain period of time after absorption t_d, the field gradient is reversed such that the de-phasing terms switch sign, thus effectively time reversing the phase evolution. This creates a collective re-phasing, i.e. all phases being 0, and reemission after a storage time $t_s = 2 * t_d$.

CRIB and GEM schemes vary from one another based upon which direction the field gradients are applied to the material either transversely or longitudinally . There are a number of different systems used to implement these memory schemes including atomic vapors, REI doped crystals, and cold atoms. CRIB/GEM has proven to be quite effective, producing the highest efficiency quantum memory yet observed [26]. This method shows long storage times, and a number of different wavelengths for operation depending on the atomic medium used. The limiting factors of these types of reversible quantum memory are the limited bandwidth, and their multi-mode storage capacity, which scales linearly with the optical depth of the medium[33]. In addition, these memories require the engineering of precise external electric or magnetic field gradients, which increases the complexity of the experiments.

3.2.4 Atomic Frequency Comb

AFC quantum memory takes full advantage of the inhomogeneous broadening found in solid-state atomic media. The inhomogeneous broadening of an atomic ensemble is related to the different magnetic and electric environments experienced by the ions that are doped into a transparent crystal. These different environments shift the energy levels of the individual ions and thus the level splitting. Each ion's individual transition has its own Lorentzian shaped homogeneous line-width [24]. When these lines are summed together over all atoms in the medium, they create an in-homogeneously broadened spectrum of the same dipole transition in the atom, but with each individual ion having a unique resonance frequency. This broadened ensemble of ions can then absorb light or single photons that span a wider range that just the homogeneous transition linewidth of individual ions. By tailoring this in-homogeneously broadened absorption spectrum we can create a quantum memory where any absorption will be followed by a reemission.

As mentioned in Section 2.4, we can use optical pumping on a three level system to modify the atomic population amongst the ground levels of ions. This effect in conjunction

with the in-homogeneously broadened spectrum in a crystal, means that we can shape the absorption spectrum of the material by pumping population out of the ground state and into the auxiliary level at specific frequencies. This is similar to the process of tailoring a sharp absorption line in the CRIB scheme discussed above. For the AFC protocol, as seen in Fig. 3.3, we seek to create a comb like structure within the absorption line of the material [35]. The characteristics of this comb feature, such as its width, depth, and tooth spacing or shape determine the various figures of merit for storage of classical or quantum light.

When a single photon is absorbed by the AFC it again creates a Dicke state[36]. Similar to the CRIB scheme above, the ensemble begins to de-phas, and the dephasing rates are given by the frequency detuning of each atom. Since the atoms have been tailored to have periodic detuning,

$$\delta_j = n_j \Delta \tag{3.7}$$

we can describe the generic de-phasing term from the Dicke state as a product of some integer n_j and the tooth spacingΔ. The Dicke state becomes

$$|\psi\rangle = \sum_{j=1}^{N} c_j e^{i2\pi n_j \Delta t_s} e^{-ikz_j} |g_1 ... e_j ... g_N\rangle, \tag{3.8}$$

and after a storage time $t_s = 1/\Delta$, all the phases become equal modulo 2π leading to a collective reemission. The efficiency for forward reemission assuming Lorentzian comb teeth, η, of a given atomic frequency comb is given by

$$\eta = (d_1/F)^2 e^{-7/F^2} e^{-d_1/F} e^{-d_0} \tag{3.9}$$

where d_1 is the optical depth of the tooth peaks, d_0 is the optical depth in the comb troughs, and F is the comb finesse, the ratio between tooth width and spacing, see Fig. 3.3. This expression suggests that for a given optical depth there exists an optimal comb finesse that produces the highest efficiency storage $\eta_{max} = 54\%$ for forward emission. For backwards emission, and additional phase matching condition or an optical cavity can be used to raise

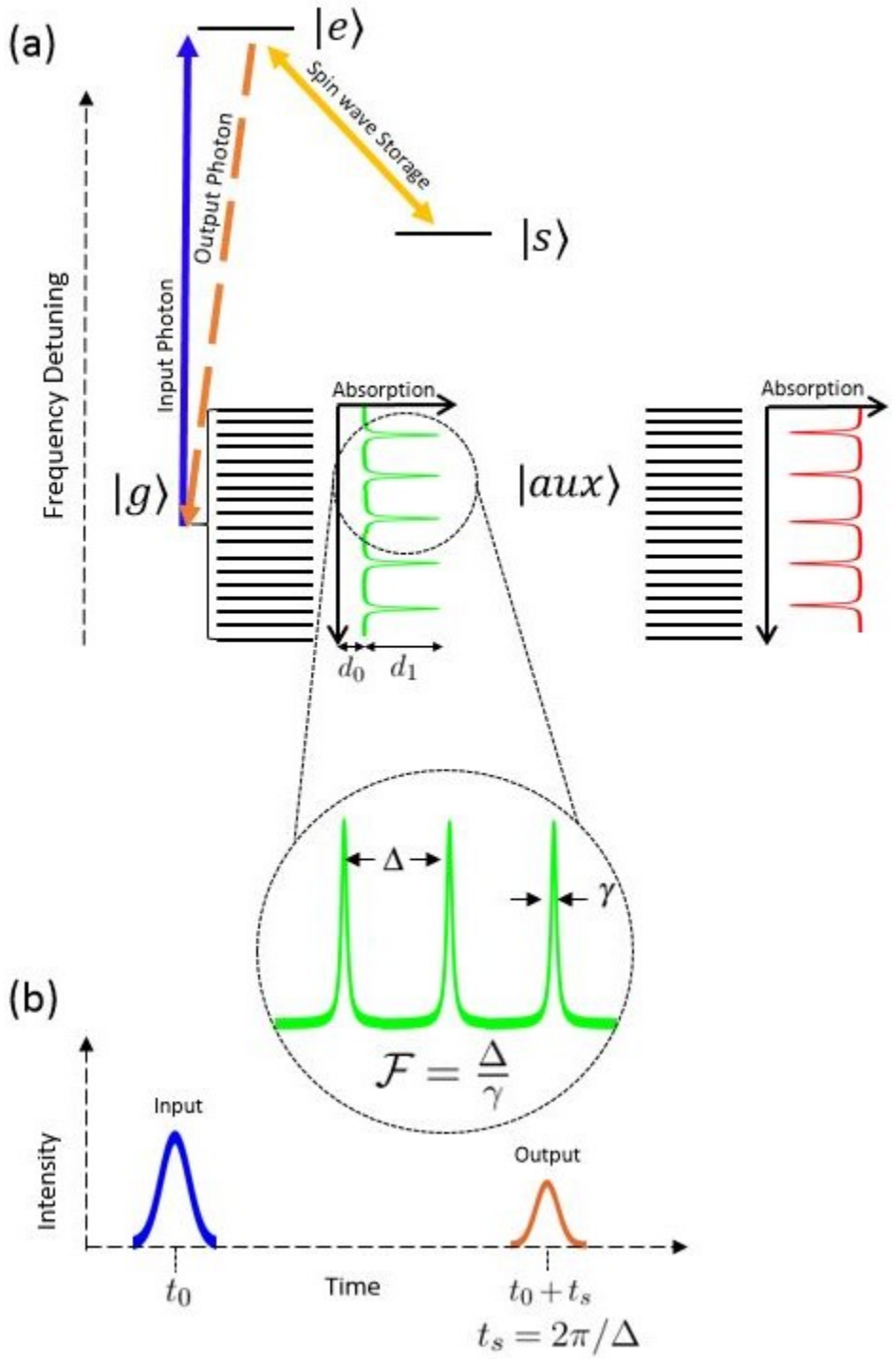

Figure 3.3: The Atomic Frequency Comb scheme for storage. Shown here are the in-homogeneously broadened ground and auxiliary states $|g\rangle$ and $|aux\rangle$. The population of atoms with particular transition frequencies is optically pumped into the auxiliary level to form a comb-like structure. The teeth spacing Δ of this comb determines the storage time while the finesse $\mathcal{F}$, dependent on the ratio between teeth spacing and tooth width γ, partially determines the efficiency of the memory. The optical depth of the comb teeth and troughs are denoted d_0 and d_1. Figure adapted from [35]

the memory efficiency arbitrarily close to 1 [37]. Lastly, efficiency is limited by decoherence effects on the population of ions during storage.

The storage time of the AFC memory protocol is fixed once the comb tooth spacing, Δ, is created via optical pumping, but on-demand storage is possible using a spin level, different from the shelving level, of the same ensemble. In this case, sometime before the collective re-phasing, a secondary optical π-pulse on resonance with a transition to a spin state, is applied to the memory. The pulse transfers the atomic excitation between excited and ground states to an excitation between the ground-spin levels, which generally feature a longer coherence and lifetime. This stops the dipole de-phasing process and stores the quantum state for up to the coherence time of thespin transition involved in the storage. For retrieval, at any time later, another optical pulse can be sent to the memory to transfer the excitation back out of the spin state, and continue the re-phasing on the ground-excited level AFC for eventual reemission. These processes, both for fixed time and on-demand storage, have been demonstrated in a number of different materials [38, 39, 40, 32].

By the figures of merit above, the AFC scheme is attractive for many different applications. The multi-mode capacity for the quantum memory is independent of the material's optical depth, meaning the potential for multiplexing is hindered only by the width of the materials inhomogeneous broadening, which can be as large as 300 GHz in crystals such as Tm:$LiNbO_3$. The bandwidth for storage depends on the width of the optical pumping, the magnetic fields available, and sometimes the spacing of the hyperfine levels of the material. Storage times for the AFC range between a few nanoseconds to milliseconds. Similarly AFC quantum memories have been implemented in materials where the working wavelength is useful for many applications. These memories make a good candidate for the future of quantum communications and quantum information so they are the implementation which we use to store quantum correlations in the experiments described by this thesis.

Chapter 4

Quantum Memory and Photon Generation Experimental Setups

We have covered why we seek to perform this experiment and the physics behind AFC quantum memories. Now we will describe how we store quantum correlations carried by two photons in quantum memories based in different REI doped materials. The experimental setup requires many different complex components to run in sequence with one another. We begin with a photon pair source that creates our correlated photons, one each at the transition wavelength for the two AFC quantum memories. Each individual memory setup must then store one of the single photons and regurgitate it at the correct time without disturbing the quantum state of the original photon pair. Finally, there are a number of details in the detection of these single photons and their timing that allows us to observe their quantum correlations. I will discuss briefly how each of these different portions work, and how we optimized the different components together to produce our results.

4.1 Entangled Photon Pair Source

For generation of the stored light, we have built an entangled photon pair source based on Spontaneous Parametric Down Conversion (SPDC). This source begins with a 1047 nm laser pulsed at an 80 MHz clock rate. This clock signal will also help us perform temporal filtering for the detected photons. The 6 ns-long pulses are then sent through a Second Harmonic Generation(SHG) step in a nonlinear crystal to produce higher-energy 523 nm light pulses of 15 ps length [41]. Once the higher-energy pulses are created, the beam is directed into a periodically poled Lithium Niobate nonlinear crystal to generate photon pairs at the working

Figure 4.1: The SPDC pair source. 6 ns long pulses of 1047 nm light, with an 80 MHz repetition rate, are sent to a SHG crystal and converted to 15 ps long pulses of 523 nm. The pulses of 523 nm light are directed into another nonlinear crystal. It is temperature stabilized, to produce by SPDC pairs of photons resonant with the transitions in erbium doped fiber (1532 nm) and thulium lithium niobate (795 nm). These single photons are split by wavelength on a dichroic mirror, and then sent through narrow bandwidth optical cavities to assure their spectra fall within range.

wavelengths for both memories using SPDC [42, 43]. From energy conservation we can see,

$$\frac{1}{523nm} \approx \frac{1}{795nm} + \frac{1}{1532nm}, \tag{4.1}$$

meaning the wavelengths of the photon pairs produced by this setup match the transitions of each REI doped material. This wavelength pairing is tunable over a small range with the temperature of the nonlinear crystal, which alters the internal phase matching condition, and the allowed wavelengths for photon pair generation. After splitting the produced photon pairs by their wavelength on a dichroic mirror, we have two spatially isolated yet temporally and spectrally correlated single photons. These single photons are spectrally filtered using high-finesse optical cavities such that only photons matching the memory transition frequencies can be coupled into optical fibers for use in the memories. Note that we can also introduce a Mach-Zender Interferometer for the pump light to create time bin qubits, [44, 45].

We characterize the photon statistics of the light produced by this source, see Fig.4.2, using the normalized cross correlation function $g_{12}^{(2)} = \frac{\langle I(t)_1 I(t)_2 \rangle^2}{\langle I(t)_1 \rangle \langle I(t)_2 \rangle}$, which describes the probability of simultaneous field detections [46]. From the definition of the Cauchy-Schwarz R

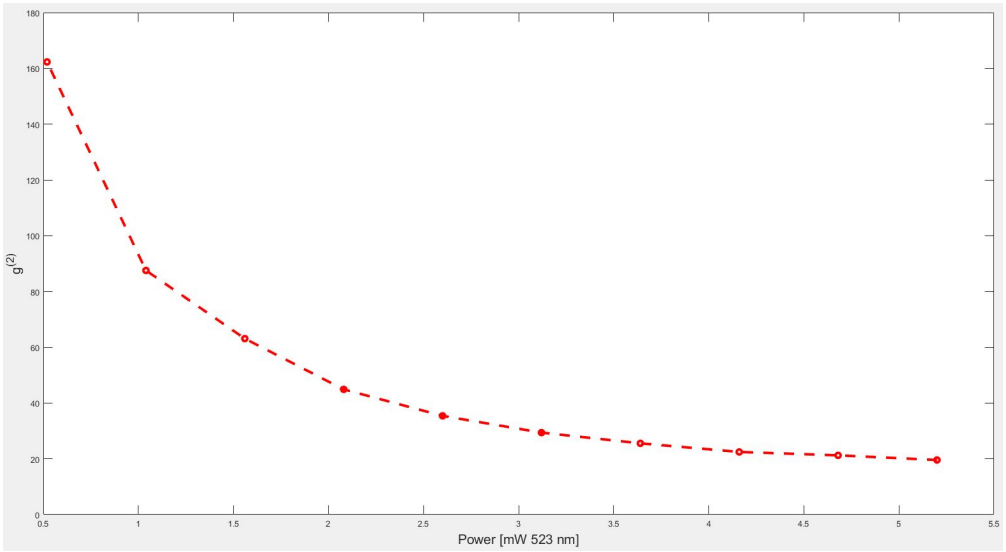

Figure 4.2: $g^{(2)}$ of the entangled photon pair source versus pump power after SHG.

parameter,

$$R = \frac{(g_{12}^{(2)})^2}{g_{11}^{(2)} g_{22}^{(2)}} \leq 1 \tag{4.2}$$

we can see that certain values of the correlations functions characterize non-classical effects that violate this inequality. The photon statistics of the light produced from either arm of an SPDC source has been demonstrated to produce a bounded autocorrelation function $1 \leq g_{11,22}^{(2)}(\tau) = \frac{\langle I(t)I(t+\tau)\rangle}{\langle I(t)^2\rangle} \leq 2$ [47]. The worst case scenario is if both arms of the source are producing thermal light with auto correlation functions of exactly $g_{11,22}^{(2)} = 2$. For the correlations between the two arms to be non classical, the normalized cross correlation function must then be $g_{12}^{(2)} \geq 2$, making $R \geq 1$. For the bare source, we measure $g_{12}^{(2)} \approx 20$ using maximum pump power, clearly demonstrating its non-classical character [48]. This cross correlation value increases as we lower the power of the pump laser and produce a lower average number of photon pairs from the nonlinear crystal, thereby decreasing the probability of emitting more than one pair.

The single photons created in this setup are detected by a set of superconducting nanowire single-photon detectors (SNSPD). These detectors have efficiencies above 80%, low jitter

around 100 ps, and dead times of roughly 100 ns [17]. The single photon detection signals are amplified, lengthened, and sent to analysis electronics to determine if the single detections should trigger a coincidence count. In order to filter noise from dark counts, the raw detection signals for one of the detections are electronically AND-gated with the clock signal of the source pump laser. This ensures that only single photons generated by the laser pulses are used for data collection. Once the timing of the detection pulses are correctly defined, using delay generators, the signals are sent to a time to digital converter (TDC) for precise time tagging. The TDC has a collection window of 160 ns, so a photon detection for one half of the pair AND-gated with the clock signal starts the collection window, and then a second detection from another detector acts as a stop signal ending the collection. After analysis, the TDC data produces a histogram plot with 2000 bins, each 80 ps wide, that displays the coincidence detection signals from this source and eventually from the memories.

4.2 The Thulium Memory Setup

The single photons at 795 nm, created as described above, are sent through optical fibers to our thulium quantum memory setup. There, an AFC quantum memory is created in a Tm:$LiNbO_3$ crystal through an optical pumping sequence. The crystal itself, a small rectangular sample, is held in a cryostat capable of cooling the crystal down to approximately 600 mK to give us access to the required energy level structure without any dynamics or rapid decoherence. There are two optical paths that address this crystal: one for optical pumping to create the spectral comb structure, and the other to send and retrieve the single photons to be stored.

The optical pumping light, centered at 795 nm, is created with an extended cavity diode laser. The wavelength is tuned to address a small bandwidth portion of the in-homogeneously broadened transition from 792-796 nm within the Tm:$LiNbO_3$. Shown in Fig.4.3, the continuous wave (CW) light is coupled into optical fiber for mode cleaning, and then pulsed

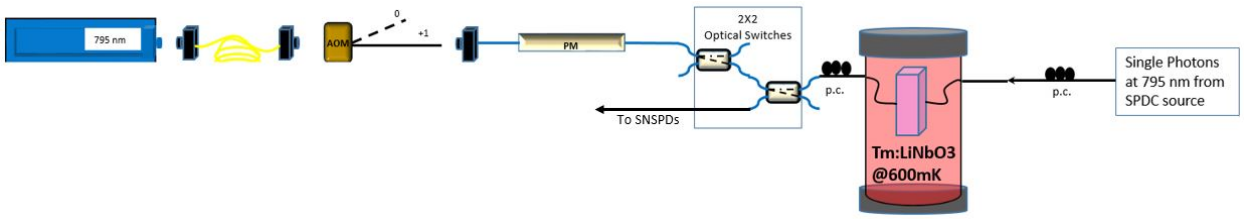

Figure 4.3: The thulium quantum memory setup. A CW diode laser at 795 nm is mode cleaned in fiber, and sent to an AOM to quickly pulse the light. The first order path of this AOM is directed into a fiber-coupled EO Space phase modulator which frequency shifts the light to create different peaks in the pulses' power spectrum. After a set of optical switches to direct the burning light and single photons, the pump light is sent to the Tm:$LiNbO_3$ crystal in our cryostat to create an AFC. The single photons travel from our source through a polarization controller (PC) to the memory for storage. When they are regurgitated, they are routed through an optical switch to the SNSPDs. All the different elements are controlled by a sequence generator that triggers and drives the different elements with the correct duty cycle.

using a 400 MHz acousto-optic modulator (AOM) which is driven by RF signals generated by the sequence electronics. Burning pulses arise from the first order diffraction path of the AOM, while the remaining zeroth order AOM light is used to monitor the laser frequency stability. Before directing a burning pulse into the crystal, the pumping light is frequency shifted throughout the desired bandwidth of the AFC memory.

The frequency of the burning light is shifted by a phase modulator (PM). The phase modulator receives a sawtooth electrical signal, amplified from an Arbitrary Waveform Generator(AWG), to create an optical serrodyne frequency shift for the wavelength of the input light [49]. With this modulation and shifting technique, the power spectrum of light becomes a comb of closely spaced peaks. Each of these different peaks of light burns a gap, or transparency window, in the in-homogeneously broadened absorption spectrum of the Tm:$LiNbO_3$ corresponding to a trough between AFC teeth. The storage time for the Thulium memory was chosen to be 32 ns, thus a peak spacing of $\Delta = 1/(32ns) = 31.25$ MHz is required between the peaks of the AFC. Using this method we create a finesse 2 comb using 1 mW of input power.

The resulting light pulses are directed through a polarization controller to create optimal interaction with the thulium ions. The pumping pulses are routed through a set of two micro electro-mechanical switches (MEMS) to allow for different optical paths addressing the same mode, and into the cryostat via an optical fiber. Using a glass capillary tube, a ferrule and a grin lens to collimate the beam from the fiber, the pumping light is directed through the Tm:$LiNbO_3$ crystal. A second optical fiber couples out of the crystal in the same manner, yielding approximately 20% coupling of the pump light collected through the output fiber. Both coupling fibers are on translation stages with nano-meter precision in three dimensions to allow movement for the best possible coupling efficiency. This coupling efficiency was maintained throughout all measurements.

For creation of the AFC, seen in Fig.4.4, we send 20 burning pulses, each with a duration of 1 ms into the memory. We characterize the comb by measuring the optical depth of the peaks and troughs in relation to the total optical depth of the Tm:$LiNbO_3$ at this wavelength. We measure a trough optical depth of $d_0 = 0.75 \pm 0.25$ and a peak optical depth of $d_0 + d_1 = 2.95 \pm 0.15$, each of which depends on laser stability, the efficiency of our frequency shifting process, and the magnetic field used to create the level splittings in the thulium. According to (3.9), for a finesse 2 comb, these OD's produce an estimated memory efficiency of 3-4%.

The efficiency stated here is limited by a number of experimental parameters. The laser stability, and our technique for burning and frequency shifting both lower the efficiency of the comb that we can produce. Additionally the magnetic field in the experiment partially determines the effects of the burning pulses on the absorption spectrum of the material. Since certain experimental parameters must match the setup for the erbium fiber, they are not made optimal for the memory efficiency on the thulium side. The optimization process for these related parameters will be discussed in Section 4.4.

The second optical path leading to the Tm:$LiNbO_3$ quantum memory is for the stored

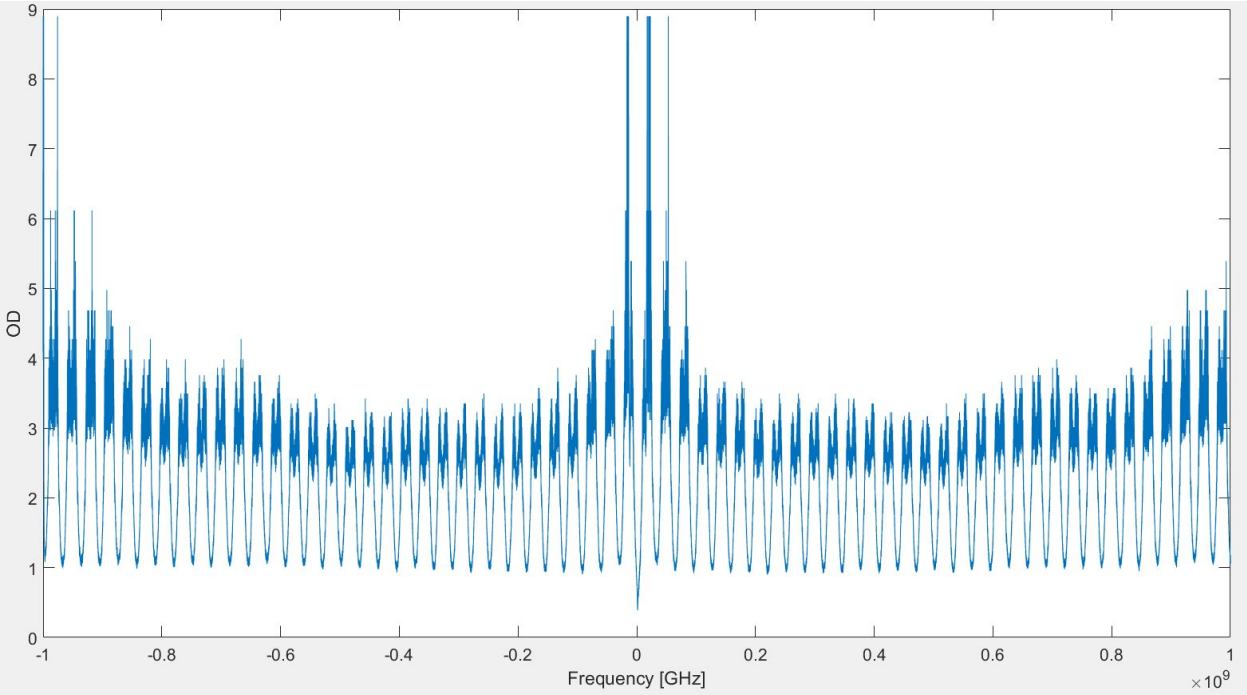

Figure 4.4: Example of the thulium AFC. To produce this picture, once an AFC has been created by our optical pumping, weak light is swept across the comb feature and then detected in time. This is a 2 GHz sample from the center of the comb where the burning process is most efficient. The storage efficiency of this comb is approximately 2.5%, which can be determined by the depth of the troughs and by the height of the peaks. Note the unintentional double peaked nature of each tooth. This leads to multiple storage times of the comb at 32 and 64 ns.

photons. The single photons from the entangled photon pair source are directed through a polarization controller and sent into the memory. The polarization of the single photons is matched to the polarization of the burning light and the orientation of the thulium ions' transition dipole moment in the crystal for the most efficient storage. After absorption, the photons are re-emitted after 32 ns and they travel through the MEMS for routing to the SNSPDs for analysis.

4.3 The Erbium Memory Setup

The single photons generated at 1532 nm are sent to a quantum memory implemented in an erbium doped optical fiber also held at 600 mK. This wavelength is tuned to address a small portion of the in-homogeneously broadened transition from 1530-1536 nm within the erbium absorption spectrum. Erbium doped glass fiber has already been demonstrated to store single photons and quantum entanglement [40]. This memory is also addressed by two optical paths running both directions through the fiber, one to burn an AFC in the absorption profile of the erbium ions, and the other to send single photons to be stored. These two paths operate similarly to those in the other memory.

The optical pumping path creates CW light centered at 1532 nm using a extended cavity diode laser that is then coupled into optical fiber. A PM to tailor the power spectrum of the light into many equally spaced frequency peaks is the next component. In contrast to the thulium setup, a polarization scrambler then allows the pump light polarization to be swept over all angles quickly. This is used to address all the different classes of ions in the amorphous erbium doped fiber material compared to the ordered thulium crystal. The pumping light is then sent through a fiber AOM and an optical switch for pulsing the burning light with high extinction ratio. Finally, a circulator, is used to route the burning light and single photons correctly during different parts of the experimental cycle. The light for pumping the erbium memory is all controlled in fiber so there is little to no coupling loss

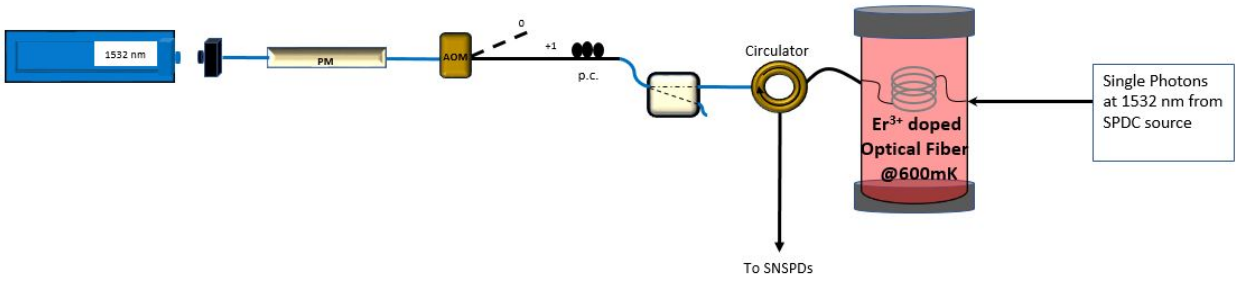

Figure 4.5: Erbium quantum memory setup. The light from a CW laser at 1532 nm is coupled into fiber and sent to a PM for frequency shifting. Followed by an AOM for creating burning pulses and an optical switch for increased extinction ration, the light is sent through a circulator and into the cryostat to create a memory in the erbium atoms isolated in the optical fiber. When storing single photons they are sent back through the fiber, and directed to the single photon detectors. The length of erbium doped fiber in the cryostat is 20 m, resulting in a transmission time of 100 ns without storage.

between the pump light and the memory fiber since the burning setup is spliced to the fiber memory. The laser frequency and output power are monitored with an optical cavity and detectors to ensure laser stability throughout the experiment. Single photons run into the erbium doped fiber for storage. Upon reemission, they travel out of the third port of the circulator to the SNSPDs.This setup can be seen in Fig.4.5.

The frequency spectrum of the light is shaped to produce periodic peaks of optical power every 167 MHz, corresponding to a storage time of 6 ns for the created AFC. This is again a finesse 2 comb, created by 1000 pumping pulses of the frequency-shifted light each 500μs long. Since the memory is not a single monolithic crystal but a 20 m fiber, the whole length of which has been doped with Erbium ions, there is both a storage time, and a transmission time for the memory. The storage time of the atoms is a result of a collective excitation spread across the erbium ions at all points in the fiber. For the 20 meters of fiber, it takes light 100 ns to transmit through the memory medium. This leads to a total optical delay of 106 ns for single photons stored using the erbium doped fiber. An example of the comb created by this setup is given by Fig. 4.6.

We were able to create combs with a trough optical depth of $d_0 = 2.25 \pm 0.15$ and peaks

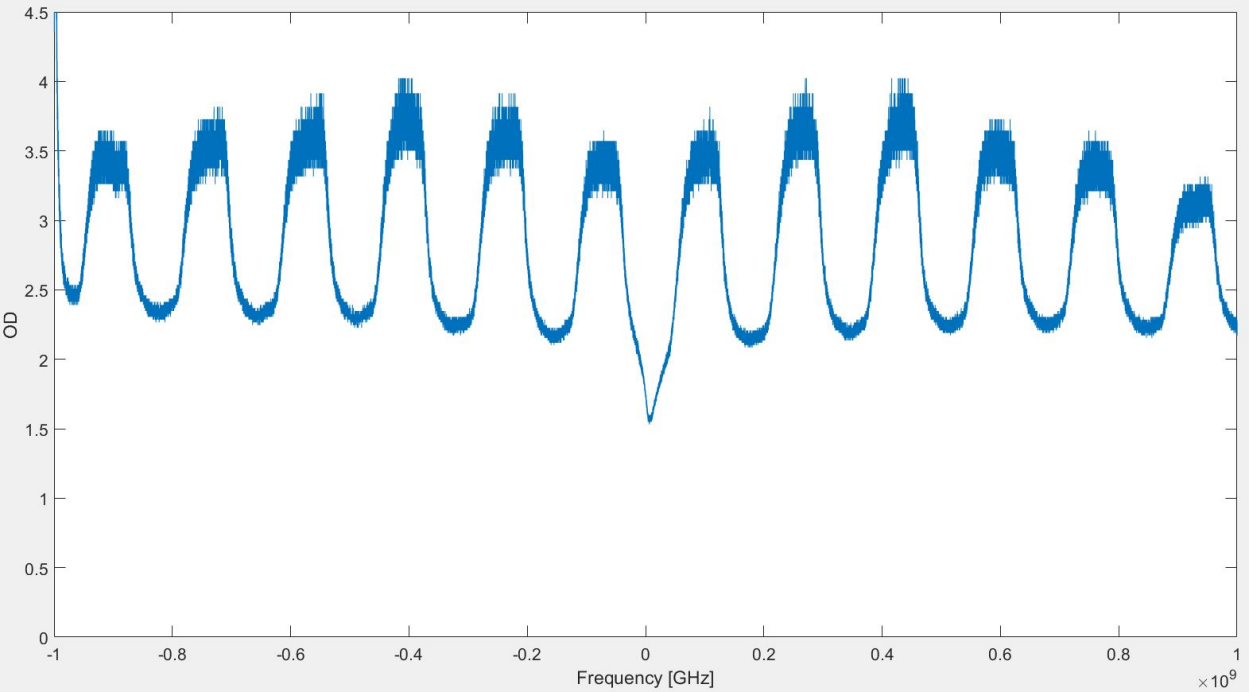

Figure 4.6: Example of the erbium AFC scan. To produce this spectrum, weak light is swept across the created comb feature and then detected. This is a 2 GHz sample from the center of the comb where it is most efficient. The efficiency of this comb is approximately 0.5%, which can be determined by the depth of the troughs and peaks of the teeth. The storage time for the comb pictured is 6 ns.

with an optical depth of $d_0 + d_1 = 3.85 \pm 0.25$. These numbers vary with the pumping laser stability, and the temperature of the erbium doped fiber when we were able to burn the comb. These numbers for optical depth produce an estimated memory efficiency of 0.5-1% for a finesse 2 comb. This memory could not be fully optimized as some key parameters, i.e. the magnetic field, are shared between between both memories, and must be optimized for the experiment as a whole.

4.4 Optimization

The dual optimization and synchronization needed to get both memories working together changes the ideal working parameters used for each memory. Minor bits of optimization included maximizing couplings and splicing fibers to reduce optical loss, but major improvements were still needed to observe our results. We began the dual optimization and synchronization process with the least efficient memory, the erbium fiber.

The erbium fiber memory requires a low magnetic field due to the high value for the splitting of the Zeeman levels used for storage. Above 1500 Gauss, the efficiency of the possible erbium AFCs to be burned falls with the magnetic field strength. This threshold remains constant over all wavelengths in the range of the erbium ions absorption spectrum. The efficiency of the thulium memory rises with higher magnetic field, so this efficiency loss in the erbium memory sets a hard limit on the maximum magnetic field to be used in the experiment.

Storage time was the next consideration for optimization of the results. In the case of erbium, there is a major loss in memory efficiency with storage times longer than 10 ns. A storage time of 6 ns was selected to be a decent balance of efficiency and duration, in conjunction with the transmission time of the fiber. This storage time also places the photon echo peak from the erbium memory in a relatively low-noise temporal location on the analysis histograms. The storage efficiency in the erbium memory proved fairly insensitive to

changes in pumping wavelength for this field and storage time so we fixed those parameters and switched to finding optimal conditions at this magnetic field for the thulium crystal.

For thulium in the 1500 Gauss magnetic field, different storage times at different wavelengths were examined, and compared to the estimated AFC efficiency that we could create. This analysis showed the best storage time and wavelength combination to be 794.698 nm with a 32 ns storage time. The wavelengths of the stored single photons must match the wavelength for the burning light such that the single photons fall in the bandwidth of the created AFC. Aligning the source to generate one part of the photon pair at 794.698 nm meant the corresponding photon to be stored in the erbium memory would need to be at 1533.1 nm. Thus the SPDC energy conservation sets the wavelength for comb burning in the erbium memory. The product of the two estimated memory efficiencies was the parameter that we attempted to maximize, in this case coming to the maximum value of $0.79_{Er}\% * 3.41_{Tm}\% = 2.7 \times 10^{-2}_{total}\%$.

Our next optimization step was to improve not just the estimated AFC efficiency, but the rate of echo signals detected in first runs of the system. We did this by increasing the number of single photons from the source incident on the memories. In the initial setup, the 795 nm photons produced by the source are filtered by an optical cavity with 6 GHz transmission bandwidth. This drastically reduces the number of photons incident on the memory even though this bandwidth is theoretically aligned with the AFC storage bandwidth. For the thulium memory, to increase the rate of incident photons, we removed this optical cavity and began performing the spectral filtering with the AFC memory itself. This increased the thulium memory echo rate four fold without increasing the detected noise. Only photons in the spectral bandwidth of the AFC memory are detected at the correct 32 ns delayed time. All other photons incident on the Tm:$LiNbO_3$ crystal may be absorbed by the material and then re-emitted as spontaneous emission at random times in random directions. These spontaneous emissions have potential to be noise counts, but they are mostly filtered out due

to the direction of their emission being misaligned with our memory output fiber. With only the AFC for spectral filtering, the echo signal is proportional to the AFC bandwidth. This set the thulium memory AFC Bandwidth at 8 GHz, close to the maximum we could create, as the frequency shifting of the phase modulator becomes inefficient at higher bandwidths.

The erbium fiber functions with the highest possible echo signal-to-noise ratio when the 10 GHz optical filter cavity of the source is in place. Removing the filter cavity was not possible on the erbium memory side because the erbium fiber is itself a waveguide. When absorbed (unfiltered) photons again cause spontaneous emission, those randomly directed emissions are preferentially captured by the waveguide nature of the fiber, and directed to the detectors creating intractable noise levels. The bandwidth of the erbium memory was set at 10 GHz to match the bandwidth of the filter cavity, and produce maximum echo signal.

To remove any other excess noise in the experiment, we synchronized the duty cycles of both memory setups. To optically pump the erbium ions, a burning period of 500 ms was required. This burn time is followed by 200 ms of waiting time as some spontaneous emission, leftover from the pump light, dies down. During this whole 700 ms period the SNSPDs are gated off so as not to contribute noise counts. The experimental time for storage and retrieval of single photons is then another 700 ms during which the detectors are gated on to collect data and the pumping light is switched off. For the Thulium experimental cycle, the burning time is 20 ms, with 5 ms of waiting time. The experimental time is the same 700 ms, during which both memories are collecting data for photons that are part of correlated pairs. The trigger signals for both memories are synchronized such that the experimental times overlap exactly. This reduces the noise counts from starting signals that do not belong to correlated single photons.

We calculated the timing for the paths of the single photons. Lengths were adjusted such that photons created in the same correlated pair reach the two memories 5 ns apart. The 1532 nm photon arrives at the erbium fiber approximately 5 ns before the 795 nm photon arrives

at the Tm:$LiNbO_3$ crystal. Storage begins for both memories when the photons arrive, meaning that if both photons from a given pair are stored, they share 32 ns of simultaneous storage in the two memories. With this optimized setup in place, we built our way towards measuring coincidences between echo photons from both memories.

Chapter 5

Results

We started measurements by checking some preliminary results. There were a number of different configurations to test while building up to coincidences between echo photons from both memories.

5.1 Intermediate Results

The first preliminary setup was a looped-looped configuration in which the single photons from the source run through longer fibers straight to the detectors, thereby bypassing both memories. This configuration leads to roughly the same coincidence detection rates as the source itself, but with a bit extra loss introduced by the longer fiber paths traveled by the photons. This produces a histogram, seen in Fig.5.1, that is started by the 1532 nm photon AND-gated with the clock signal, and stopped by any detection signal of a 795 nm photon. The histogram trace produced by this setup has a single clear coincidence peak that we center at zero using electronic delay generators. There are additional coincidence detections between different clock cycles. These detections are termed accidental peaks, and can be seen every 12.5 ns on the histogram, corresponding to the 80 MHz clock rate of the source pump laser. This histogram serves as our baseline for detections, and by adding more experimental components we add features to the plot such as additional noise, and signal peaks from the recalled photons.

The next configuration step was to include only one memory at a time in a looped-echo or echo-looped configuration. This is a heralded detection of echo photons from a single memory. One memory produces an echo while the other photon of the pair bypasses its memory. We configure the electronics so that the looped side detection signal, AND-gated

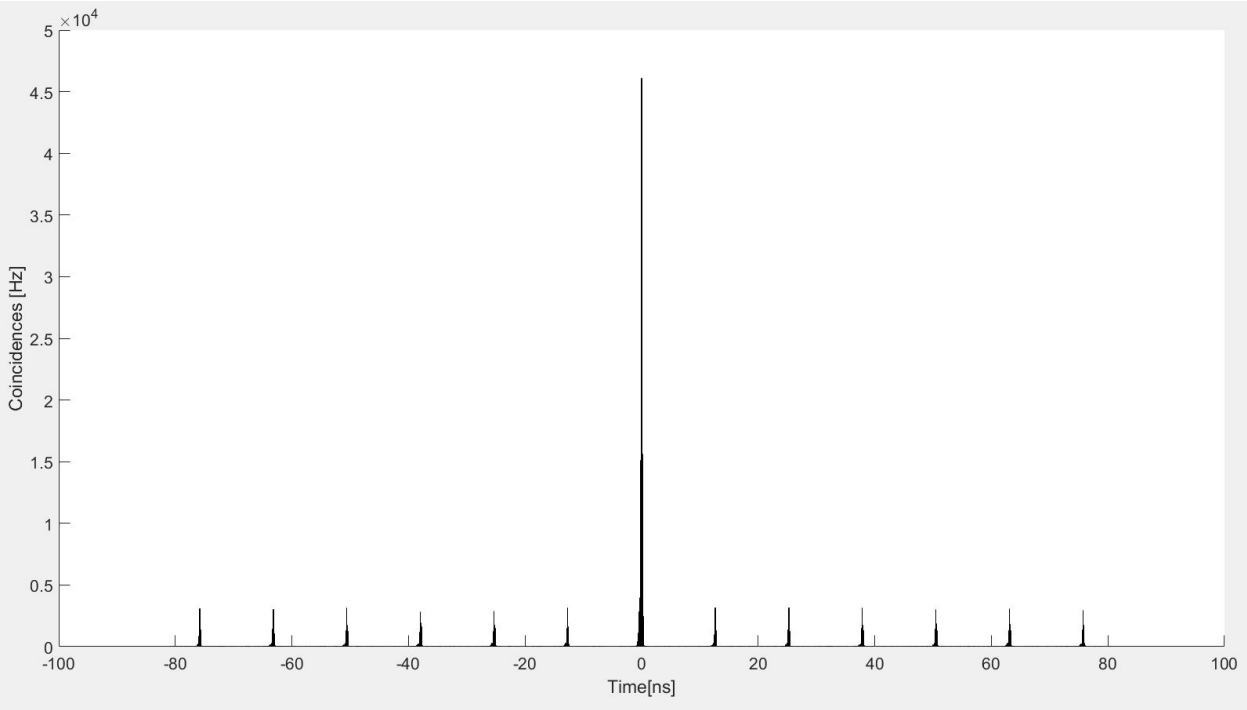

Figure 5.1: Pictured here is a looped-looped histogram trace produced by the analysis electronics. The large peak at the center is the peak of all coincidence detections in one clock cycle between the pairs of 795 nm and 1532 nm single photons. Electronic delay generators are set to place these coincidence detections at the center of the collection window. The second feature of this plot are the accidental peaks. These are the detection coincidences that span different clock cycles, such that one photon from a first pair, and one from a later pair are detected coincidently.

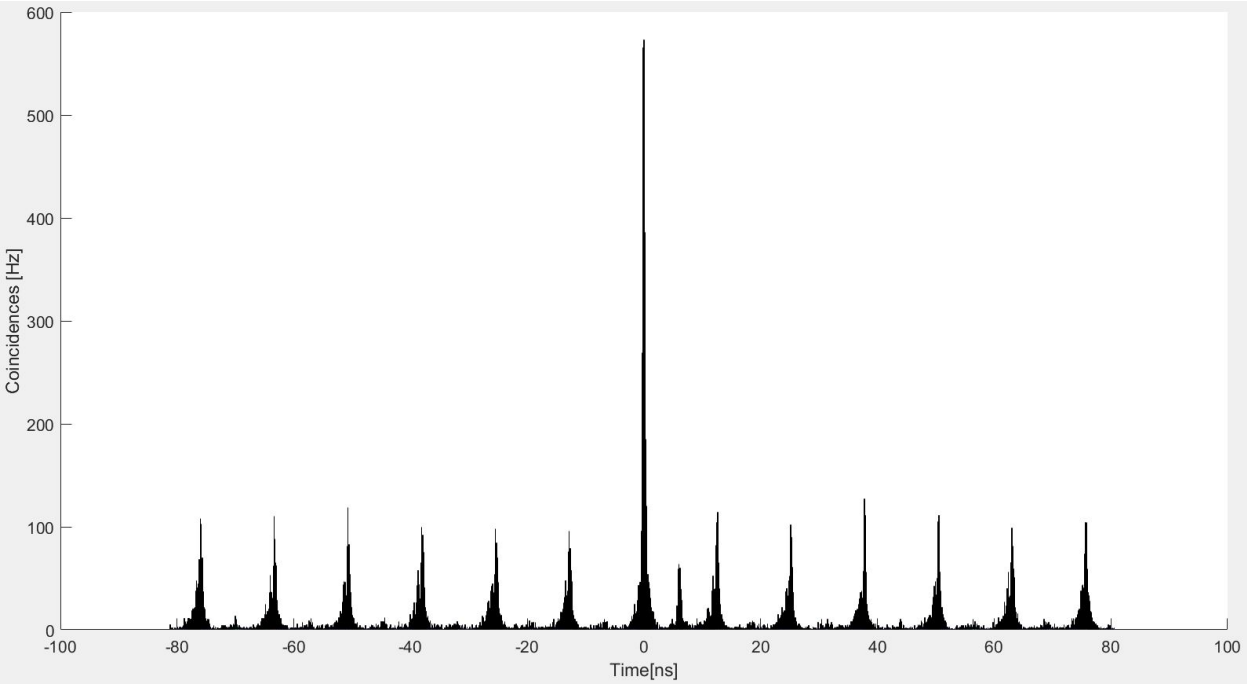

Figure 5.2: This is a histogram produced in the echo-looped configuration taken over the span of 10 minutes. There is the usual histogram structure with the center transmitted coincidence peak, and the corresponding accidental peaks from various clock cycles. The additional peak delayed exactly 6 ns from the direct transmission peak are the photon echo detections produced by the AFC memory in the erbium doped fiber. The erbium memory efficiency is low, so the number of dark counts is closer to the number of counts for the signals seen here. This effect, and the presence of any spontaneous emission leftover from the burning process, serves to make the signals fuzzier in this histogram compared to Fig. 5.1 above.

with the clock starts the data collection, and photons coming from the working memory produce the stops, both as transmitted or echo photons. This produces histograms that look like Fig. 5.2 and Fig.5.3 for erbium and thulium, respectively, as the active memory. The histograms for these configurations are clear evidence of the echoes produced by both memories of photons produced by the SPDC source.

With clear echoes from both sides of the experiment, we moved on to measure the complete experimental setup, and its increased loss. The next pair of signals is created by photons transmitted through the memory setups, but not stored, and the echo photons of the opposite memory. This decreases the heralding signal due to the loss from the coupling

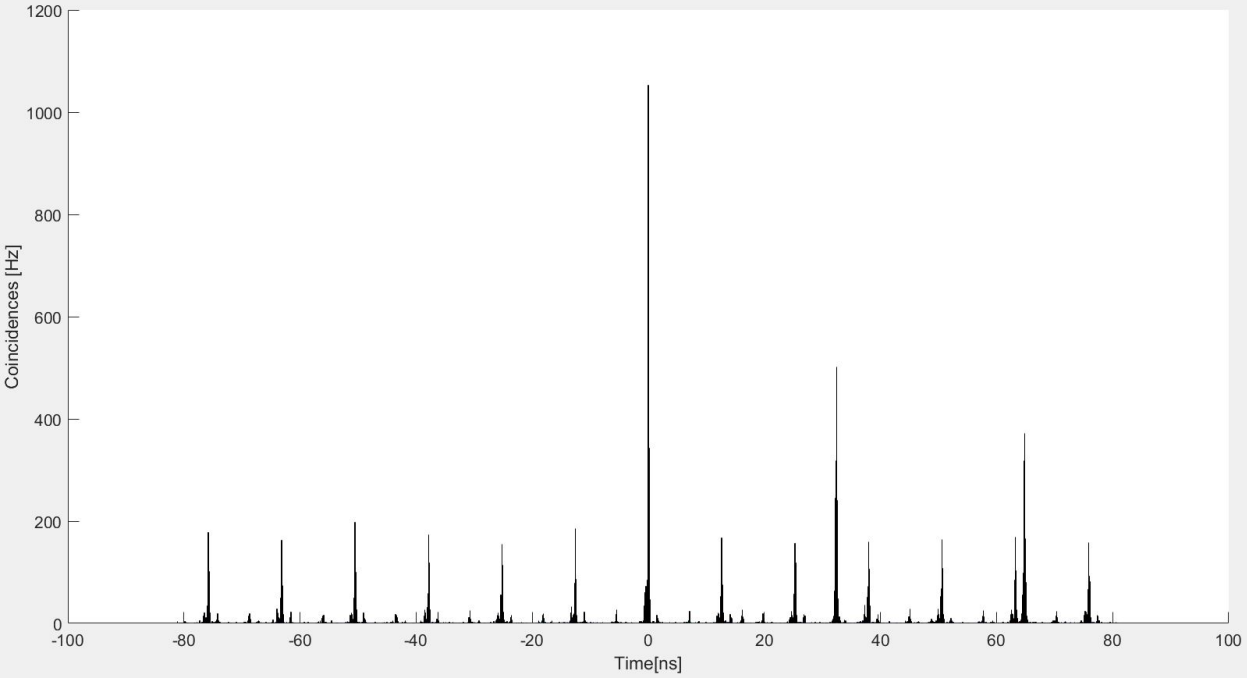

Figure 5.3: This is a histogram produced in the looped-echo configuration taken over the span of 10 minutes. The usual structure is evident in this histogram, but so are two additional photon echo peaks. The echo peaks occur exactly at 32 ns and 64 ns delayed from the direct transmission peak, corresponding to the different frequency components of the double peak feature in the thulium AFC. The clarity of the signal is much better than the erbium echo signal. There is much less spontaneous emission noise from the thulium memory, and, since the efficiency is higher, the echoes appear much higher above the background.

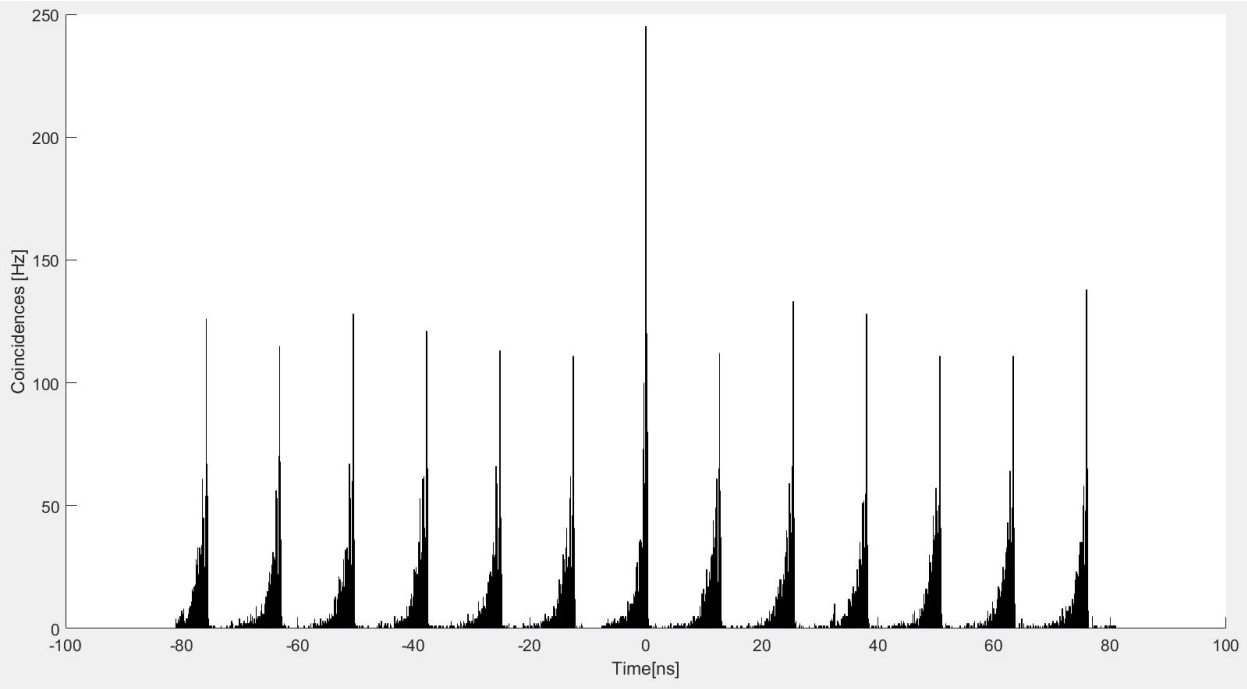

Figure 5.4: This is a transmitted echo trace taken over the span of 10 minutes. The signal shown here is for the thulium memory echo, and the first feature to notice is the reduced count rate. Even for the transmitted peak there is a factor of 4 fewer counts than in the trace from Fig. 5.3. The echo peak at 32 ns is still barely visible, but this histogram illustrates how close the experiment is to a signal to noise ratio of 1. Note the asymetry in the detection peaks comes from the imperfect collection bins of the TDC.

optics and fiber of one setup, while still detecting the photon echo from the other memory side. A histogram from this configuration is shown in Fig. 5.4. The effects of the extra loss are clearly apparent in this histogram. There are fewer counts in the same amount of time, including a reduction in the echo signal. While the switching from looped-echo to transmitted-echo accounts for some loss, switching again to echo-echo coincidences amounts to adding even more. The probability of joint detections are reduced to the product of the system efficiencies of each memory setup. This takes into account the same losses of the transmitted configuration but each signal is reduced again by the efficiencies of the memories. This results in extremely low count rates, but nonetheless we are able to detect echo-echo coincidences with long collection times.

5.2 Echo-Echo coincidence and g(2) Measurements

The final steps for the work in this thesis are to measure echo-echo coincidences between photons stored in both memories simultaneously and to measure the $g^{(2)}$ cross correlations between those photons . To perform the first measurement we alter the conditions for the start and stop signals for the data collection. In the case of a transmitted-echo configuration, the start signal is the detection of a transmitted photon AND-gated with the clock signal. These electronic signals are aligned with each other using a set of electronic delay generators. For echo-echo coincidences, we use the delay generators to align the clock signal with the time of which there should be an echo detection signal from the erbium fiber. Thus photons detected 6 ns after the transmitted peak are AND-gated with the clock signal and produce a start for data collection. In principle this is only echo photons from the erbium memory, but there are certainly also some dark counts and other noise that occur in this window that lead to spurious starts. The stop signal is again any photon detected on the detector for 795 nm photons. This will produce multiple stop peaks, one for each photon transmitted through the Tm:$LiNbO_3$, photons from the first stored echo, and photons from the secondary echo. With this detection system in place we found that echo counts would occur roughly once a minute. After hours of data collection, we produce a histogram similar to the ones above, which is shown in Fig. 5.5.

We next verified the nature of these signals. To make sure that the peaks arise from stored single photons that may share quantum correlations, and not noise, we compare the histogram in Fig. 5.5 with data taken after moving the echoes signals away from these temporal windows where we have measured the correlations. For this analysis we moved the echoes to 8 ns in the erbium memory and to 34 ns in the thulium memory and measured only the noise that remained in the temporal windows at 6 ns and 32 ns. With only the thulium echo displaced, we take the same echo-echo trace to find the number of noise counts in the echo window. Comparing the signal trace to the noise trace we see a signal to noise ratio

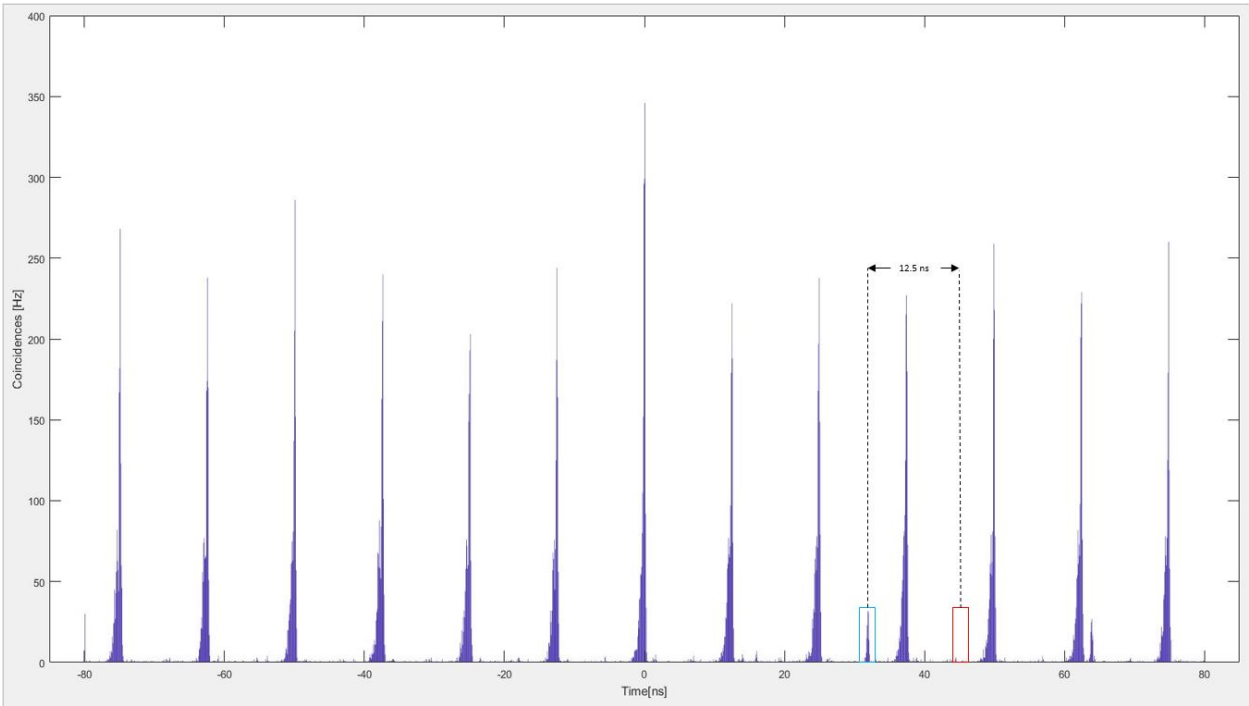

Figure 5.5: This is a histogram produced by the sum of 160 minutes of data collection for the echo-echo configuration. Starts for this data are photon echoes from the erbium memory and the clock signal, while stops are detections from 795 nm photons. There is the usual structure of the center peak, with the periodic accidentals. There are also peaks corresponding to the echo detections at 32 ns and 64 ns. These peaks are coincidence detections between echo photons from both memories. The regions corresponding to the coincidence signal (blue) and the accidental window for another clock cycle (red) are shown.

(SNR) of 120 in that temporal window. Using a similar method for the erbium echo we find an SNR of 2.05 and the data from these noise trace measurements is included in Appendix B. The starts with the erbium memory echo displaced do not create any temporal structure beside the 80 MHz clock signal. This means that though we do have noise at a comparable level on the 1532 nm photon detector, those noise photons are random dark counts that happen to occur in conjuction with the clock signal. These noise detections are uncorrelated with any stop photon detections and do not contribute to our final $g^{(2)}$ measurement.

The quantum correlations seen between the SPDC photons are temporal, so the clear timing in Fig.5.5 suggests their non-classical temporal correlations were kept intact throughout the storage process. We can determine $g^{(2)}$ from the ratio of the detection counts measured from the traces above,

$$g_{12}^{(2)} = \frac{C_{12}}{C_1 * C_2} \tag{5.1}$$

where C_{12} are the coincidence detection counts per second in a 0.5 ns window, and C_1 and C_2 are the single counts of each individual detection arm per second. Their product, $C_1 * C_2$, can also be expressed by the accidental coincidences in the correct temporal window[50]. Hence, to measure the $g^{(2)}$ function, it suffices to measure the ratio of the coincidences to accidentals (CAR) in the corresponding histogram windows, see Fig.5.5. We average the accidentals in this window over many clock cycles to determine an accurate accidental count rate $C_1 * C_2$. From the signal produced in the histogram above for the echo-echo coincidences at 32 ns we find $g^{(2)} = 16 \pm 2$. The classical limit of 2 for the $g^{(2)}$ function is violated here by 7 standard deviations, thus we can conclude that we have stored and re-emitted single photons that share non-classical correlations [18, 48, 51]. This result shows clearly that the non-classicality of the correlations between the light fields was preserved during the simultaneous storage of both photons in truly quantum memories.

Chapter 6

Outlook

We have shown with the experiment presented above that we are able to store non-classical correlations in quantum memories based on materials that operate at two different wavelengths. This is the first step towards demonstrating a functional interface between different quantum memories. Using this system, or one with the improvements presented below, we will be able to make stronger claims about the memories that we have connected, and the quantum states that they share.

6.1 Improvements

The experiment described above clearly connects the quantum memories that we use, but would not translate to use in a real-world application without improvement. We are not limited in our ability to detect these quantum correlations, but there is still a long way to go for systems such as ours to be useful in a real-world quantum information context. The clearest path towards use is through improvement of the quantum memories. The storage times used for both quantum memories are quite short compared to the ones needed for applications. We demonstrate simultaneous storage for 32 ns while a real quantum network or quantum computer interface could require storage times on the order of at least a few hundred μs. This limitation in our setup is partially due to the materials in which we have created our AFC memories, but there is ongoing research into improved erbium and thulium materials [52, 53]. Even for our current thulium memory, we do not take full advantage of the available storage time because of the shared magnetic field in our setup.

The second major improvement needed for this experiment is due to the total experimental efficiency. We obtained our results with rates of roughly one count per minute. Classical

communications and computers currently have information transfer rates on the order of hundreds of gigahertz. We need to improve all lossy aspects of the experiment to improve the rate of detections for real-world applications. This could include an improved photon pair source with higher coincidence count rates, higher efficiency fiber coupling and detectors, improved memory efficiency, or multiplexing for multiple spectral channels. There is a proposal for improvement of the AFC memory efficiency through an impedance matched cavity scheme which has demonstrated success in other materials [37, 38]. Similarly, using multiplexing to perform storage over more frequency channels is well understood and has shown capacity for improvement of counting rates in AFC quantum memories[54]. With these improvements in place, potential applications for a quantum memory interface as demonstrated above become more feasible.

6.2 Next Steps

We will take this experiment to the next step by showing quantum effects that imply a deeper relation between the memories during photon storage. There is a clear recipe for showing what types of different quantum states persist during storage [55, 40]. The first step in proving the applications and usefulness of our quantum system is to use qubits instead of just correlated single photons. We will add a Mach-Zender interferometer to our single photon source to create time-bin qubits out of the single photons generated by SPDC. For the analysis of these qubits, we will also add phase stabilized interferometers in addition to our single photon detectors to determine the state returning from the memories. A stronger statement than the sharing of non-classical correlations is to say that we have stored entanglement and demonstrated non-locality between the two quantum memories.

Since entanglement can not be generated by local operations alone, then if the photons are part of an entangled state after being emitted from the memories, the atomic excitations in each memory must have been entangled with one another during the simultaneous

storage. Using different measurement combinations for the analysis interferometers, we will perform quantum state tomography, and a measurement of certain correlation coefficients to evaluate the CHSH inequality. The density matrix will show the entanglement of our state by determining various entanglement measures such as the tangle and concurrence [56, 57]. The CHSH inequality will show that a local hidden variable theory could not explain our results [58]. The full realization of this experiment, once it has shown entanglement and non-locality of the states stored in the memories, will be another crucial proof of principle result for the interfacing of different quantum information systems at a distance.

6.3 Looking Ahead

We have shown that entanglement and the beneficial properties of qubits can translate between quantum systems that operate at different wavelengths. With time and effort, results such as these will lead to connections between different implementations of qubits and diverse quantum networks that span greater distances across the globe. The classical Internet is now a broad and ever changing web of connections. Years ago it may have only included a few computers or nodes but it has blossomed to connect different types of devices and users across the world. Fostering these early quantum connections of disparate quantum devices over larger and larger distances can be the only strategy for improving the quantum information infrastructure that will one day lead to a quantum Internet.

Appendix A

Quantum Memory Comparison

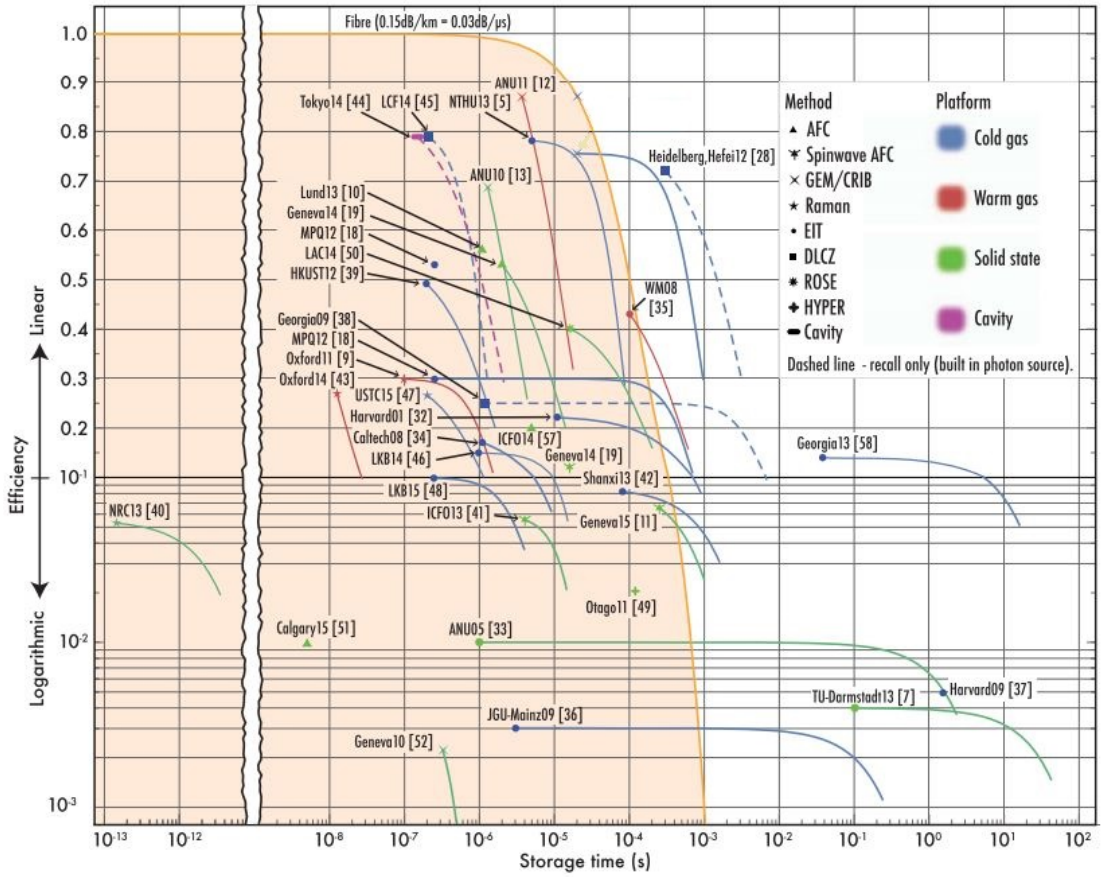

Figure A.1: Taken directly from [26] this figure gives a summary of many of the different quantum memory experiments performed. This is a a plot of only two figures of merit discussed above, but it gives a good sense of the many different implementations. This plot does not account for many of the figures of merit which make the AFC scheme for quantum memory, especially the ones here in Calgary, beneficial, such as bandwidth and multimodal capacity. The yellow shaded area on the plot indicates the effective times and efficiencies where an optical fiber delay line acting in place of the memory would be more effective.

Appendix B

$g^{(2)}$ Noise Measurements

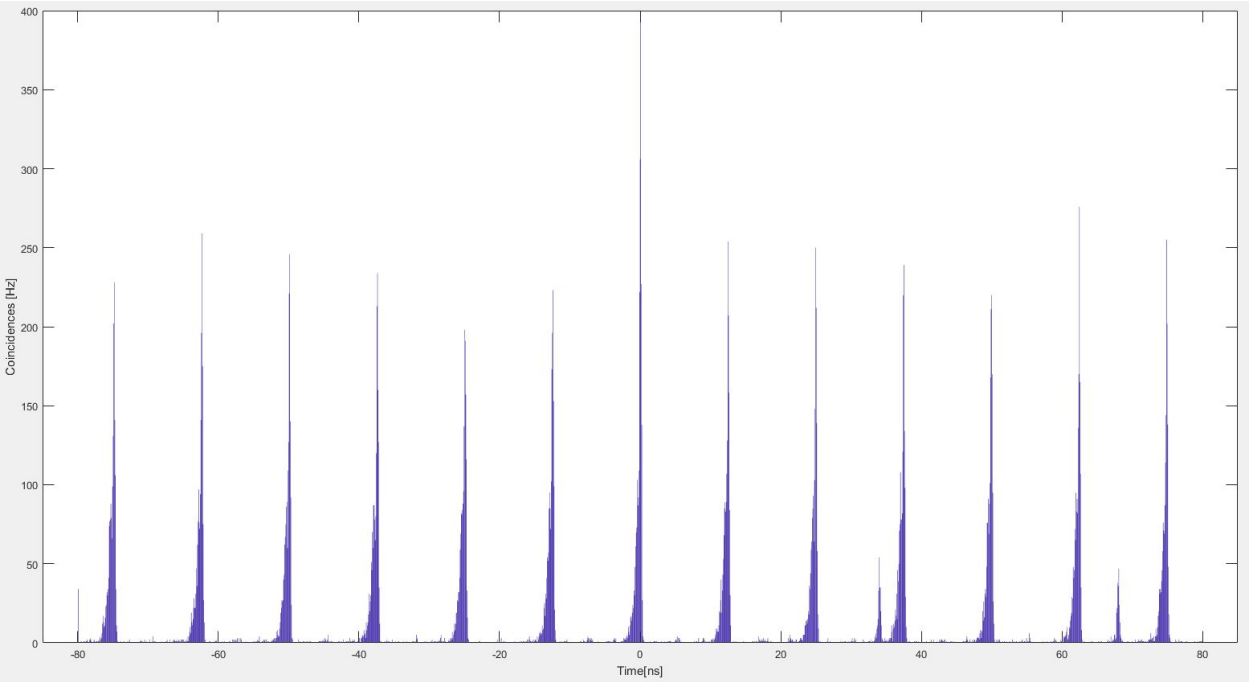

Figure B.1: Histogram taken with the Thulium echo moved to 34 ns. The TDC starts are still taken from an Erbium memory echo at 6 ns. With the echo shifted, the detection signals come at 34 ns leaving only 1 count of noise where the echo used to be at 32 ns.

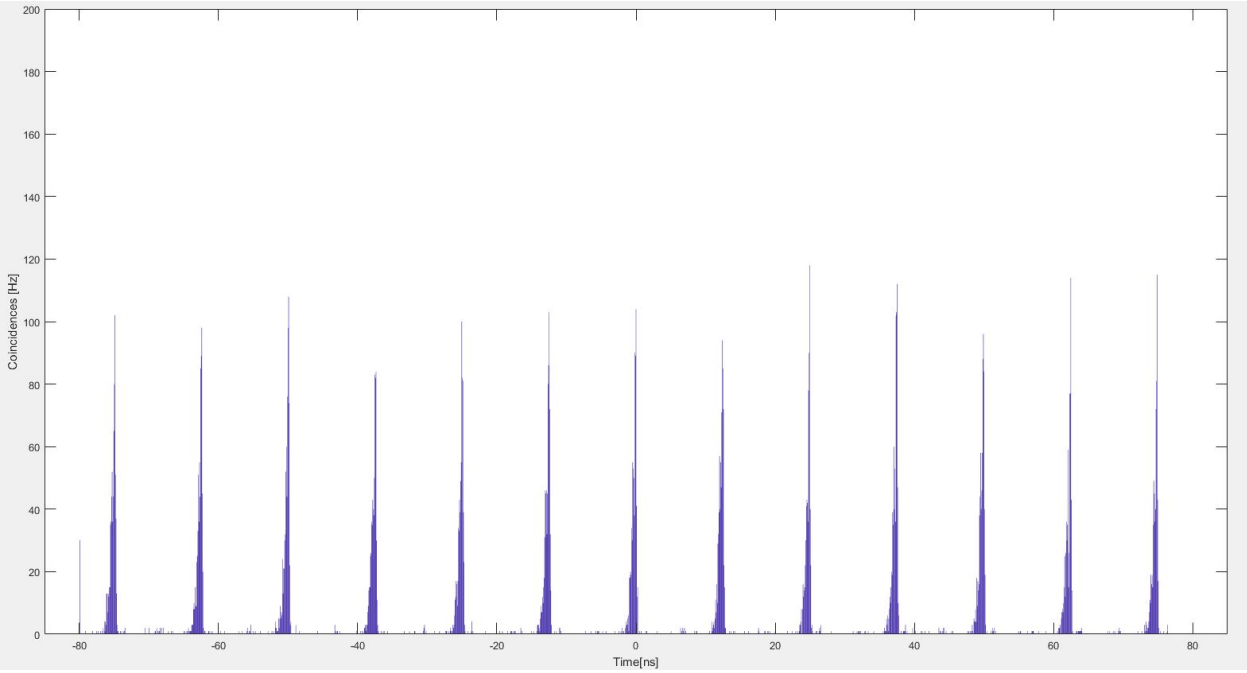

Figure B.2: Histogram taken after the erbium echo was moved to 8 ns. Now the TDC is started by the clock signal ANDed with noise present at 6 ns, not with a recalled photon. Hence, start signals due to detected photons arise with equal probability every 12.5 ns, but no coincidence peak due the detection of both photons from the same pair is visible.

Bibliography

[1] A. Einstein, B. Podolsky, and N. Rosen, "Can quantum-mechanical description of physical reality be considered complete?," *Phys. Rev.*, vol. 47, pp. 777–780, May 1935.

[2] J. P. Dowling and G. J. Milburn, "Quantum technology: The seond quantum revolution," *https://arxiv.org/abs/quant-ph/0206091*, 2002.

[3] P. Shor, "Polynomial-time algorithms for prime factorization and discrete logarithms on a quantum computer," *SIAM J. Comput.*, vol. 26, pp. 1484–1509, Oct. 1997.

[4] N. Gisin, G. Ribordy, W. Tittel, and H. Zbinden, "Quantum cryptography," *Rev. Mod. Phys.*, vol. 74, pp. 145–195, Mar 2002.

[5] M. A. Nielsen and I. L. Chuang, *Quantum Computation and Quantum Information: 10th Anniversary Edition*. Cambridge: Cambridge University Press, 2010.

[6] D. P. DiVincenzo, "The physical implementation of quantum computation," *Arxiv*, 2000.

[7] M. H. Devoret and R. J. Schoelkopf, "Superconducting circuits for quantum information: An outlook," *Science*, vol. 339, no. 6124, pp. 1169–1174, 2013.

[8] H. J. Kimble, "The quantum internet," *Nature*, vol. 453, pp. 1023–1030, June 2008.

[9] N. Gisin and R. Thew, "Quantum communication," *Nat Photon*, vol. 1, pp. 165–171, Mar. 2007.

[10] H. Hübel, M. R. Vanner, T. Lederer, B. Blauensteiner, T. Lorünser, A. Poppe, and A. Zeilinger, "High-fidelity transmission of polarization encoded qubits from an entangled source over 100 km of fiber," *Opt. Express*, vol. 15, pp. 7853–7862, June 2007.

[11] L.-M. Duan, M. D. Lukin, J. I. Cirac, and P. Zoller, "Long-distance quantum communication with atomic ensembles and linear optics," *Nature*, vol. 414, pp. 413–418, Nov. 2001.

[12] L. Childress and R. Hanson, "Diamond nv centers for quantum computing and quantum networks," *MRS Bulletin*, vol. 38, no. 2, pp. 134–138, 2013.

[13] N. Sinclair, E. Saglamyurek, M. George, R. Ricken, C. L. Mela, W. Sohler, and W. Tittel, "Spectroscopic investigations of a Ti:Tm:$LiNbO_3$ waveguide for photon-echo quantum memory," *Journal of Luminescence*, vol. 130, no. 9, pp. 1586 – 1593, 2010.

[14] Y.-H. Chen, X. Fernandez-Gonzalvo, and J. J. Longdell, "Coupling erbium spins to a three-dimensional superconducting cavity at zero magnetic field," *Phys. Rev. B*, vol. 94, p. 075117, Aug 2016.

[15] N. Maring, P. Farrera, K. Kutluer, M. Mazzera, G. Heinze, and H. de Riedmatten, "Photonic quantum state transfer between a cold atomic gas and a crystal," *Nature*, vol. 551, p. 485, 2017.

[16] S. Tanzilli, W. Tittel, M. Halder, O. Alibart, P. Baldi, N. Gisin, and H. Zbinden, "A photonic quantum information interface," *Nature*, vol. 437, p. 116, Sep 2005.

[17] M. Eisamana, J. Fan, A. Migdall, and S. Polyakov, "Invited review article: Single-photon sources and detectors," *Review of Scientific Instruments*, vol. 82, no. 7, 2011.

[18] J. F. Clauser, "Experimental distinction between the quantum and classical field-theoretic predictions for the photoelectric effect," *Phys. Rev. D*, vol. 9, pp. 853–860, Feb 1974.

[19] G. Liu and B. Jacquier, *Spectroscopic Properties of Rare Earths in Optical Materials*. Springer, 2005.

[20] E. Saglamyurek, T. Lutz, L. Veissier, M. P. Hedges, C. W. Thiel, R. L. Cone, and W. Tittel, "Efficient and long-lived zeeman-sublevel atomic population storage in an erbium-doped glass fiber," *Phys. Rev. B*, vol. 92, p. 241111, Dec 2015.

[21] P. Bushev, A. K. Feofanov, H. Rotzinger, I. Protopopov, J. H. Cole, C. M. Wilson, G. Fischer, A. Lukashenko, and A. V. Ustinov, "Ultralow-power spectroscopy of a rare-earth spin ensemble using a superconducting resonator," *Phys. Rev. B*, vol. 84, p. 060501, Aug 2011.

[22] Y. Sun, C. W. Thiel, and R. L. Cone, "Optical decoherence and energy level structure of 0.1% Tm^{3+}:$LiNbO_3$," *Phys. Rev. B*, vol. 85, p. 165106, Apr 2012.

[23] F.X.Kaertner, "6.977 ultrafast optics lecture notes," Chapter 2, 2005.

[24] L.Allen and J. Eberly, *Optical Resonance and Two-Level Atoms*, vol. 28. 1975.

[25] F. Bloch, "Nuclear induction," *Phys. Rev.*, vol. 70, pp. 460–474, Oct 1946.

[26] Y.-W. Cho, G. T. Campbell, J. L. Everett, J. Bernu, D. B. Higginbottom, M. T. Cao, J. Geng, N. P. Robins, P. K. Lam, and B. C. Buchler, "Highly efficient optical quantum memory with long coherence time in cold atoms," *Optica*, vol. 3, pp. 100–107, Jan 2016.

[27] W. Tittel, M. Afzelius, T. Chaneliére, R. Cone, S. Kröll, S. Moiseev, and M. Sellars, "Photon-echo quantum memory in solid state systems," *Laser & Photonics Reviews*, vol. 4, no. 2, pp. 244–267, 2010.

[28] A. I. Lvovsky, B. C. Sanders, and W. Tittel, "Optical quantum memory," *Nature Photonics*, vol. 3, p. 706, 2009.

[29] C. Simon, M. Afzelius, J. Appel, A. Boyer de la Giroday, S. J. Dewhurst, N. Gisin, C. Y. Hu, F. Jelezko, S. Kröll, J. H. Müller, J. Nunn, E. S. Polzik, J. G. Rarity, H. De Riedmatten, W. Rosenfeld, A. J. Shields, N. Sköld, R. M. Stevenson, R. Thew,

I. A. Walmsley, M. C. Weber, H. Weinfurter, J. Wrachtrup, and R. J. Young, "Quantum memories," *The European Physical Journal D*, vol. 58, pp. 1–22, May 2010.

[30] R. de L. Kronig, "On the theory of dispersion of x-rays," *J. Opt. Soc. Am.*, vol. 12, pp. 547–557, Jun 1926.

[31] M. Bajcsy, A. S. Zibrov, and M. D. Lukin, "Stationary pulses of light in an atomic medium," *Nature*, vol. 426, p. 638, Dec 2003.

[32] K. Heshami, D. G. England, P. C. Humphreys, P. J. Bustard, V. M. Acosta, J. Nunn, and B. J. Sussman, "Quantum memories: emerging applications and recent advances," *Journal of Modern Optics*, vol. 63, no. 20, pp. 2005–2028, 2016.

[33] J. Nunn, K. Reim, K. C. Lee, V. O. Lorenz, B. J. Sussman, I. A. Walmsley, and D. Jaksch, "Multimode memories in atomic ensembles," *Phys. Rev. Lett.*, vol. 101, p. 260502, Dec 2008.

[34] B. Kraus, W. Tittel, N. Gisin, M. Nilsson, S. Kröll, and J. I. Cirac, "Quantum memory for nonstationary light fields based on controlled reversible inhomogeneous broadening," *Phys. Rev. A*, vol. 73, p. 020302, Feb 2006.

[35] M. Afzelius, C. Simon, H. de Riedmatten, and N. Gisin, "Multimode quantum memory based on atomic frequency combs," *Phys. Rev. A*, vol. 79, p. 052329, May 2009.

[36] P. A. Zarkeshian, C. Deshmukh, N. Sinclair, S. K. Goyal, G. H. Aguilar, P. Lefebvre, M. G. Puigibert, V. B. Verma, F. Marsili, M. D. Shaw, S. W. Nam, K. Heshami, D. Oblak, W. Tittel, and C. Simon, "Entanglement between more than two hundred macroscopic atomic ensembles in a solid," *Nature Communications*, vol. 8, p. 906, Oct 2017.

[37] M. Afzelius and C. Simon, "Impedance-matched cavity quantum memory," *Phys. Rev. A*, vol. 82, p. 022310, Aug 2010.

[38] M. Sabooni, Q. Li, S. Kröll, and L. Rippe, "Efficient quantum memory using a weakly absorbing sample," *Phys. Rev. Lett.*, vol. 110, p. 133604, Mar 2013.

[39] P. Jobez, N. Timoney, C. Laplane, J. Etesse, A. Ferrier, P. Goldner, N. Gisin, and M. Afzelius, "Towards highly multimode optical quantum memory for quantum repeaters," *Phys. Rev. A*, vol. 93, p. 032327, Mar 2016.

[40] E. Saglamyurek, J. Jin, V. B. Verma, M. D. Shaw, F. Marsili, S. W. Nam, D. Oblak, and W. Tittel, "Quantum storage of entangled telecom-wavelength photons in an erbium-doped optical fibre," *Nature Photonics*, vol. 9, p. 83, Jan 2015.

[41] P. A. Franken, A. E. Hill, C. W. Peters, and G. Weinreich, "Generation of optical harmonics," *Phys. Rev. Lett.*, vol. 7, pp. 118–119, Aug 1961.

[42] M. Grimau Puigibert, G. H. Aguilar, Q. Zhou, F. Marsili, M. D. Shaw, V. B. Verma, S. W. Nam, D. Oblak, and W. Tittel, "Heralded single photons based on spectral multiplexing and feed-forward control," *Phys. Rev. Lett.*, vol. 119, p. 083601, Aug 2017.

[43] J.-W. Pan, Z.-B. Chen, C.-Y. Lu, H. Weinfurter, A. Zeilinger, and M. Żukowski, "Multiphoton entanglement and interferometry," *Rev. Mod. Phys.*, vol. 84, pp. 777–838, May 2012.

[44] J. Brendel, N. Gisin, W. Tittel, and H. Zbinden, "Pulsed energy-time entangled twin-photon source for quantum communication," *Phys. Rev. Lett.*, vol. 82, pp. 2594–2597, Mar 1999.

[45] I. Marcikic, H. de Riedmatten, W. Tittel, V. Scarani, H. Zbinden, and N. Gisin, "Time-bin entangled qubits for quantum communication created by femtosecond pulses," *Phys. Rev. A*, vol. 66, p. 062308, Dec 2002.

[46] H. Paul, "Photon antibunching," *Rev. Mod. Phys.*, vol. 54, pp. 1061–1102, Oct 1982.

[47] P. R. Tapster and J. G. Rarity, "Photon statistics of pulsed parametric light," *Journal of Modern Optics*, vol. 45, no. 3, pp. 595–604, 1998.

[48] A. Kuzmich, W. P. Bowen, A. D. Boozer, A. Boca, C. W. Chou, L. Duan, and H. J. Kimble, "Generation of nonclassical photon pairs for scalable quantum communication with atomic ensembles," *Nature*, vol. 423, p. 731, Jun 2003.

[49] L. M. Johnson and C. H. Cox, "Serrodyne optical frequency translation with high sideband suppression," *Journal of Lightwave Technology*, vol. 6, pp. 109–112, Jan 1988.

[50] E. Saglamyurek, M. Grimau Puigibert, Q. Zhou, L. Giner, F. Marsili, V. B. Verma, S. Woo Nam, L. Oesterling, D. Nippa, D. Oblak, and W. Tittel, "A multiplexed light-matter interface for fibre-based quantum networks," *Nature Communications*, vol. 7, p. 11202, 2016.

[51] P. Sekatski, N. Sangouard, F. Bussiéres, C. Clausen, N. Gisin, and H. Zbinden, "Detector imperfections in photon-pair source characterization," *Journal of Physics B: Atomic, Molecular and Optical Physics*, vol. 45, no. 12, p. 124016, 2012.

[52] M. Rancic, M. P. Hedges, R. L. Ahlefeldt, and M. J. Sellars, "Coherence time of over a second in a telecom-compatible quantum memory storage material," *Nature Physics*, vol. 14, p. 50, Sep 2017.

[53] C. W. Thiel, N. Sinclair, W. Tittel, and R. L. Cone, "$Tm^{3+}:Y_3Ga_5O_{12}$ materials for spectrally multiplexed quantum memories," *Phys. Rev. Lett.*, vol. 113, p. 160501, Oct 2014.

[54] N. Sinclair, E. Saglamyurek, H. Mallahzadeh, J. A. Slater, M. George, R. Ricken, M. P. Hedges, D. Oblak, C. Simon, W. Sohler, and W. Tittel, "Spectral multiplexing for scalable quantum photonics using an atomic frequency comb quantum memory and feed-forward control," *Phys. Rev. Lett.*, vol. 113, p. 053603, Jul 2014.

[55] C. Clausen, I. Usmani, F. Bussiéres, N. Sangouard, M. Afzelius, H. de Riedmatten, and N. Gisin, "Quantum storage of photonic entanglement in a crystal," *Nature*, vol. 469, p. 508, Jan 2011.

[56] S. Hill and W. K. Wootters, "Entanglement of a pair of quantum bits," *Phys. Rev. Lett.*, vol. 78, pp. 5022–5025, Jun 1997.

[57] V. Coffman, J. Kundu, and W. K. Wootters, "Distributed entanglement," *Phys. Rev. A*, vol. 61, p. 052306, Apr 2000.

[58] J. F. Clauser, M. A. Horne, A. Shimony, and R. A. Holt, "Proposed experiment to test local hidden-variable theories," *Phys. Rev. Lett.*, vol. 23, pp. 880–884, Oct 1969.